ISAS - INTERNATIONAL SCHOOL FOR ADVANCED STUDIES

Theory of Electron Localization Function and its Applications: Surfaces, Impurities, and Enzymatic Catalysis

Thesis submitted for the degree of

"Doctor Philosophiæ"

CANDIDATE

Lorenzo De Santis

SUPERVISORS

Prof. Raffaele Resta

Dr. Paolo Carloni

October 1999

SISSA - SCUOLA INTERNAZIONALE SUPERIORE DI STUDI AVANZATI

TRIESTE
Via Beirut 2-4

TRIESTE

SISSA ISAS
SCUOLA INTERNAZIONALE SUPERIORE DI STUDI AVANZATI
INTERNATIONAL SCHOOL FOR ADVANCED STUDIES

Theory of Electron Localization Function and its Applications: Surfaces, Impurities, and Enzymatic Catalysis

Thesis submitted for the degree of
"Doctor Philosophiæ"

CANDIDATE

Lorenzo De Santis

SUPERVISORS

Prof. Raffaele Resta
Dr. Paolo Carloni

October 1999

Contents

List of Figures

Abstract

This thesis is composed of two parts, which address problems and systems rather different from each other. The common concept which provides a "leitmotiv" for the whole work is the electron localization function (ELF). In both parts of the thesis ELF is used in a nonstandard and innovative way.

ELF is a tool which is becoming these years quite much used in quantum chemistry; we provide here some of the first implementations to condensed matter, in particular within a first–principle pseudopotential scheme. We give evidence that, by focusing on the valence electrons only, one exploits at its best the spectacular insight provided by ELF into the bonding mechanisms. Notice that most of the quantum–chemical applications so far are at the all–electron level.

In the first part of this thesis we deal with bulk solids, surfaces and impurities. We demonstrate the outstanding performance of ELF in discriminating between metallic and covalent bonding, without making use of any spectral information: in fact, ELF is a pure ground–state property. Besides the actual computations for real materials, we also present a general analytical result in the framework of N-representability, where the role of ELF was not recognized so far.

In the second part we present possibly the very first application of ELF to a biochemical problem: namely, the analysis of the hydrogen bond pattern at the active site of the serine proteases, an important and large family of digestive enzymes. The ELF analysis clearly reveals that the H-bond between two key residues present at the active site can be described as a strong covalent interaction: i.e. a "low–barrier" hydrogen bond. This finding may be relevant for the biological function of this class of enzymes, helping shade new light on the quantum–chemical processes governing the catalytic mechanism.

Part I

Electron Localization Function in Condensed Systems

Introduction

Localization and its antonym, delocalization, are two words with quite a range of meanings in chemistry and condensed matter physics. Anyhow, a rigorous "quantum mechanical" definition of these concepts is necessary to describe and understand ubiquitous chemical notions such as bonds, lone–pair orbitals, lone electrons and valence–electron charge distributions.

Standard approaches in quantum–mechanics describe the single particle energy levels of a many–electron system using molecular orbitals obtained as a combinations of atomic orbitals or localized functions. In the case of *finite* systems, the use of a localized orbitals basis–set naturally leads to the familiar chemical view of charge distribution, in terms of bonding electron pairs, lone electron pairs and localized electrons. These are very useful concepts, though basis–set dependent and therefore nonunique. Going to *infinite*—either crystalline, or disordered—systems, the reduction to localized orbitals is much less trivial, additional problems arising basically from the use of periodic Born–von Kàrmàn (BvK) boundary conditions, which are almost mandatory to describe condensed systems.

Furthermore, in condensed matter theory, related to a proper definition for the electron localization there is also the problem of a rigorous interpretation of "metallicity" or "covalency" of a given bonding region. Metals are often envisioned as containing electrons *delocalized* throughout the solid, so that the electrons are free to move from one side of the sample to another; at the opposite extreme we have covalent systems, characterized by the strong localization of valence electron–pairs (the bonding pairs) forming a singlet state. Therefore, localization properties of the wavefunction can be considered as a perspicuous signature of the bonding character: a purely delocalized state corresponds to a metallic bond, whereas a localized state implies an insulating nature of the system [1].

To attempt to better understand electron localization from a theoretical standpoint, Becke and Edgecombe recently developed the *electron localization function* (ELF) [2], which has been widely used in literature to examine localization in atoms, molecules, and solids [3–7]. The ELF is a pure ground–state property, and is basis–set independent.

Amongst other appealing virtues, basically two properties make the ELF an outstanding quantum–chemical tool to analyze the localization and bonding properties. First of all, its simplicity: an ELF plot is an immediate visualization of spatial regions of electron localization. It is in fact a dimensionless function—ranging from zero to one—which is larger where the electrons are more localized, and smaller where we expect more delocalized bonding. Secondly, the ELF is a quantitative measure of how the electron distribution—by the effect of Pauli principle—locally deviates from a "reference bosonic state", in which the Pauli statistical repulsion is ideally switched off (keeping the electron density fixed) and all the electrons lie in the same ground–state orbital.

Through these two features, ELF addresses localization and bonding in a meaningful and straightforward way: namely, ELF allows us to sharply discriminate between metallic and covalent bonding character, and at the same time to clearly individuate the spatial domains of electron localization.

The quest for an univocal definition of the "electron localization" is a long–standing one in chemistry, and the ambition to solve this problem by means of some property related to the electron density—or by the electron density itself—was followed for many years. However, all these over–simplified density–based schemes easily describe the localization pattern present in simple molecules and covalent bonded solid systems (such as the "prototypical" case of bulk silicon where the valence charge shows a maximum in the bonding region), but hardly distinguishes between metallic and covalent bond and even fails to describe localized electrons in much more complicated systems [2, 6].

The novel solution proposed by Becke and Edgecombe [2] takes into account the *pairing* of electrons, which is impossible to evaluate from the charge density *alone*. The formation of electron pairs is a consequence of fermionic nature of the electrons or, equivalently, an expression of how strongly the electrons "feel" the effects of Pauli exclusion principle.

The ELF is essentially constructed as a suitable measure of the conditional probability of finding simultaneously two parallel–spin electrons in a neighborhood of each other. This probability is encoded in the *off–diagonal* elements of the one–body density matrix (in coordinate space): therefore, the basic message coming from the ELF is that in order to get a meaningful description of the localization properties in a multielectron system we have to take into account the whole one–body density matrix and *not* only its diagonal (*i.e.* the density). By construction the ELF is a functional of charge and kinetic energy density $\tau(\mathbf{r})$, whose expression is given in terms of the one–particle (spin integrated) density matrix $\rho(\mathbf{r}, \mathbf{r}')$ as:

$$\tau(\mathbf{r}) = \frac{1}{2}\nabla_{\mathbf{r}}\nabla_{\mathbf{r}'}\rho(\mathbf{r}, \mathbf{r}')\Big|_{\mathbf{r}=\mathbf{r}'}.$$

Besides ELF, other innovative paths to electron localization and bonding are explored in the current literature. The most promising of them is probably the approach based on optimally localized Wannier functions, first pursued by Marzari and Vanderbilt [8], and on the closely related concept of "localization tensor" [9, 10]. The latter is an integrated quantity (*not* a function like ELF), and provides a quantitative measure of the global amount of localization in the ground–state wavefunction: its main ingredient is once more the one–particle density matrix ρ. More precisely, the localization tensor can be expressed as a second moment of ρ as:

$$\lambda^2_{\alpha\beta} = \frac{1}{2N}\int d\mathbf{r}\int d\mathbf{r}'\,(\mathbf{r}-\mathbf{r}')_\alpha(\mathbf{r}-\mathbf{r}')_\beta|\rho(\mathbf{r}, \mathbf{r}')|^2.$$

This quantity is finite in insulators and divergent in metals.

In the first part of this thesis (Chapters 1 to 4) we present our applications of ELF to condensed systems. In Chapter 1 we review the ELF definition and properties. ELF calculations for a few bulk systems show the perspicuous ELF ability to mark a clear distinction—without using any spectral properties—between covalent and metallic bonding environments. In Chapter 2 we show a so far unnoticed connection between ELF, the N-representability problem, and the possibility to construct a new kinetic energy explicit functional: this was published as Ref. [11]. In Chapter 3 we present the application of ELF to solid surfaces, focussing on two paradigmatic cases: semiconductor (silicon) and metal (aluminum) surfaces. For the semiconductor surface, the ELF visualizes the strong rearrangement of

the bonding pattern which accompanies the surface reconstruction: this was published as Ref. [12]. For the metal surface, the ELF clearly highlights the effect of local coordination and packing upon the nature of the electron distribution in the surface region (Ref. [13]). Finally, in Chapter 4 we present our application (Ref. [14]) to disordered systems where a combined analysis of the electronic charge density distribution and ELF allows to unambiguously classify the different kinds of electronic defects (dangling and floating bonds).

Chapter 1

The Electron Localization Function

Ubiquitous chemical concepts such as "the electron pair" or "the chemical bonding character" do not univocally correspond to any directly measurable physical quantity. However, because of their undeniable conceptual utility, clear and rigorous physical definitions are essential.

For many years the major tools used in investigating bonding at large has been the analysis of either the electronic charge density or the projected density of states. Instead, only a few years ago a very powerful tool has been introduced to deal in a quantitative way with bonding features: this goes under the name of "electron localization function" (ELF). Several appealing features make ELF the tool of choice in the study of bonding patterns: ELF is a pure ground–state property, as the density is, but it "magnifies" by design the bonding features of a given electron distribution. Furthermore, ELF is dimensionless, and allows to compare the nature of bonding in different systems on an absolute scale.

In this chapter we review the ELF definition and its outstanding ability in discriminating between different bonding features. We first discuss the effect of the pseudopotential approximation upon the ELF calculations; finally, we present some benchmark results on simple molecules and paradigmatic bulk crystals, all of them confirming the same conclusion: namely, ELF yields very meaningful, easily understandable and visually informative patterns of the chemical bond.

1.1 Definition and properties

Becke and Edgecombe approach: Taylor expansion of the pair probability

To better understand the electron localization from a theoretical standpoint, Becke and Edgecombe [2] have originally introduced a new scalar function—the electron localization function—as a measure of the *conditional probability* of finding

an electron in the neighborhood of another electron with the same spin. They considered the Taylor expansion of the (spherically averaged) parallel–spin pair probability, that for small distances appears to be quadratic in the interparticle separation $s = |\mathbf{r} - \mathbf{r}'|$:

$$P(\mathbf{r}, s) = \frac{1}{2} s^2 D(\mathbf{r}) + \cdots \tag{1.1}$$

From the pair probability curvature $D(\mathbf{r})$ they defined the ELF, conveniently ranging from zero to one, that uniquely identifies regions of space where the electrons are well localized:

$$\mathrm{ELF} = \frac{1}{1 + [D(\mathbf{r})/D_h(\mathbf{r})]^2}. \tag{1.2}$$

The normalization factor $D_h(\mathbf{r})$ is the same quantity as $D(\mathbf{r})$ calculated for the homogeneous electron gas, introduced in the definition (1.2) as a fully–delocalized reference system.

The simplest form of a wavefunction satisfying the Pauli principle is a single Slater determinant. In this case, the curvature $D(\mathbf{r})$ of the pair–distribution can be easily expressed in terms of the occupied orbitals.

Properties

By the definition of Eq. (1.2), the regions where the pair probability is low—that is where an electron has a negligible probability of seeing another electron of the same spin—are regions where the electrons are strongly localized, as occurs in bonding pairs, lone–electron pairs, or where the unpaired lone–electron of a dangling orbital is localised. In all these cases, the Pauli principle is ineffective, and the ground wavefunction is nodeless (or loosely speaking "bosonic"), yielding an ELF equal to its upper bound. Furthermore, since in the homogeneous electron gas ELF by definition equals 0.5 at any density, values of this order in inhomogeneous systems indicate regions where the electrons are highly delocalized, with a prevalent metallic character.

This function has therefore higher values in regions of space where one expects bonds and lone pairs to be, and lower values where one expects more delocalized bonding: namely, plots of ELF correspond quite well to what chemists tend to qualitatively think of as "electron spatial localization".

Kinetic energy formulation

Savin *et al.* [3] have proposed another illuminating interpretation of the same

quantity, showing how $D(\mathbf{r})$ can be simply calculated in terms of the local behaviour of the kinetic energy density, thus making no explicit reference to the pair distribution function. The physical idea is basically the following: owing to the Pauli principle, the ground–state kinetic energy density of a system of fermions is larger than the one of a system of bosons at the same density [15, 16] and ELF can be equivalently expressed in terms of the extra contribution to the kinetic energy density due to the Pauli principle.

This approach is particularly convenient for our solid state context, since we work in the theoretical framework of density functional theory (DFT)[1], where an explicit calculation of the pair correlation function is totally unfeasible. Working at the independent–particle level—the Kohn and Sham (KS) level in our investigations—and using the Savin *et al.* approach, we can express the ELF directly in terms of the KS kinetic energy density.

Savin *et al.* have shown that the curvature $D(\mathbf{r})$ in Eq. (1.2) can be interpreted as the *Pauli excess kinetic energy density*, defined as the difference between the kinetic energy density and the so–called von Weizsäcker kinetic energy functional [16]:

$$D(\mathbf{r}) = \frac{1}{2}\nabla_{\mathbf{r}}\nabla_{\mathbf{r}'}\rho(\mathbf{r},\mathbf{r}')\Big|_{\mathbf{r}=\mathbf{r}'} - \frac{1}{8}\frac{|\nabla n(\mathbf{r})|^2}{n(\mathbf{r})}, \tag{1.3}$$

where ρ is the one–body reduced (spin–integrated) density matrix. The von Weizsäcker functional provides a rigorous lower bound for the exact kinetic energy density [16] and is ordinarily indicated as the "bosonic" kinetic energy, since it coincides with the ground–state kinetic energy density of a non–interacting system of bosons at density $n(\mathbf{r})$. Therefore, $D(\mathbf{r})$ is positive semidefinite and provides a direct measure of the *local effect of the Pauli principle*. The other ingredient of Eq. (1.2) is $D_h(\mathbf{r})$, defined as the kinetic energy density of the homogeneous electron gas at a density equal to the local density:

$$D_h(\mathbf{r}) = \frac{3}{10}(3\pi^2)^{\frac{2}{3}}n(\mathbf{r})^{\frac{5}{3}}. \tag{1.4}$$

The Savin *et al.* reformulation also provides a meaningful physical interpretation: where ELF is close to its upper bound, electrons are strongly paired and the electron distribution has a local "bosonic" character.

[1] A brief account of the DFT is given in Appendix A.

It is important to remark how all the ELF plots reported in this work display vanishing ELF in asymptotic regions, or where the electronic density itself approaches zero. This is a consequence of the $n(\mathbf{r})^{\frac{5}{3}}$ denominator, vanishing much more strongly than the excess local kinetic energy (except the case where $D(\mathbf{r})$ it is *identically* zero, as in a two electron atom wavefunction).

1.2 ELF in atoms, molecules and crystals

In this section we present some benchmark calculations on various systems: namely, an isolated *pseudo*–atom, three molecules where a single, a double, and a triple covalent bond is present, and finally two paradigmatic bulk crystals. We want to analyse some typical chemical bonding kinds and demonstrate how ELF portrays these kinds.

As already stressed, all the calculations presented throughout this thesis were performed adopting a fully *ab initio* method, which has become the "standard model" in modern first–principles studies of simple metals, covalent semiconductors, simple ionic solids, and many other disparate materials [17]: DFT–LDA in its KS formulation [18–20], within norm–conserving pseudopotential approximation [21]. We therefore approximate the kinetic energy of the interacting electron system with the one of the noninteracting KS one, using in Eq. 1.3 the KS density matrix:

$$\rho(\mathbf{r},\mathbf{r}') = 2\sum_i \phi_i^{KS}(\mathbf{r})\phi_i^{*KS}(\mathbf{r}'), \tag{1.5}$$

where $\phi_i^{KS}(\mathbf{r})$ are the occupied KS orbitals. Such approximation is expected to become significantly inaccurate only in the case of highly correlated materials.

1.2.1 ELF and pseudo–atoms

The original ELF definition is an all–electron one, and has the remarkable feature of naturally revealing the entire shell structure for heavy atoms [2, 5]. Such a feature is of no interest here, since only one electronic shell (the valence one) is involved in a pseudopotential framework. This approach is nowadays routinely adopted in almost all the first–principles descriptions of real crystalline systems,

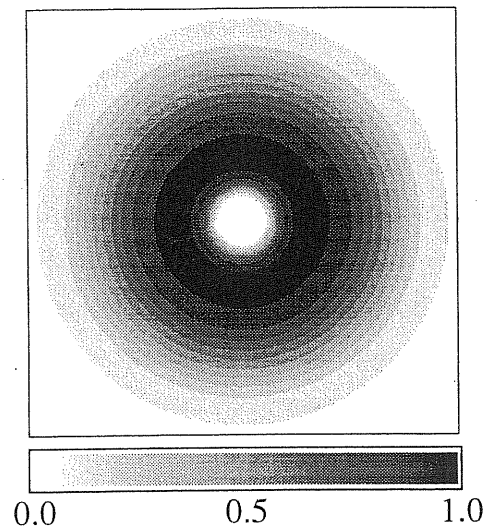

Figure 1.1: ELF for an isolated *pseudo*–atom. The grey–scale is also shown: dark (clear) regions correspond to large (small) ELF values. The same grey–scale is adopted in all subsequent contour plots.

but ELF investigations within it have been quite scarce so far. Instead, we are going to show how neglecting the core electrons and focusing solely on the bonding electrons notably simplifies the final outcome, with basically no loss of information [22] and a much clearer ELF message.

In this section, as a first example, we analyze the case of a single Al *pseudo*– atom, quoting for the moment only the effect of the pseudization upon the ELF of a general isolated atom. In a subsequent chapter, this peculiar behaviour will help us to understand the bonding pattern occurring at different Al surfaces.

Al pseudo–atom

In the spatial regions occupied by core electrons, the pseudo–electronic distribution shows a depletion and ELF assumes very low values. Outside the ionic cores, in the regions relevant to chemical bonding, the norm conservation endows the pseudocharge density with physical meaning, as widely discussed in the modern pseudopotential literature [17, 21]. By the same token of norm conservation, even the pseudo–orbitals—and hence their kinetic energy density—closely map the all–electron ones in the bonding regions. The pseudo ELF carries therefore—in the material of interest here—the same information as the all–electron ELF, while it removes irrelevant and confusing features due to the inner, chemically inert, shells.

For an all–electron atom [2, 5, 6] *each* quantum shell is associated to a visible ELF local maximum, with a clear ELF depletion between two neighboring shells. For an isolated pseudo–atom we have instead, by construction, only a *single* valence shell, clearly displayed by a single and very prominent ELF maximum. In Fig. 1.1 we report our result carried out for the Al atom: in the picture one immediately remarks the spherical region associated to the ELF maximum (0.91), where the charge density is almost bosonic. The black cloud in Fig. 1.1 indicates the strong localization of the single electronic valence shell and, as we will show in the following, perspicuously distinguishes the *free* aluminum pseudo–atom from the crystalline one.

1.2.2 ELF in molecules: covalent single, double and triple bond

As a paradigmatic example of molecular structures analyzed with ELF, we report in Fig. 1.2 the series ethane, ethylene, and acetylene where the differences between covalent single, double, and triple bonds are clearly visible.

It is well known in literature [6] how the charge density of almost all molecules is poorly structured. On the other side, all the chemical details of the structures can be clearly discerned in the ELF representation: in Figs. 1.2 (a)–(c), the C–C as well as the C–H bonding regions. The latter are diffuse and also show the position of the hydrogens.

Furthermore, an increasing contraction of the bonding region along the C–C axis is observed with increasing bond order. In the case of the ethyne, Fig. 1.2(c), there is only a localization torus around the bonding line. The maximum of the electron density is found in the mid point of C–C connecting line, but the highest ELF values are found outside: this result, first of all, confirms how a simple charge density analysis hardly describes all the chemical features of a given electron distribution. Secondarily, is in perfect agreement with the tipical description of double and triple bonds in terms of $\sigma - \pi$ orbitals.

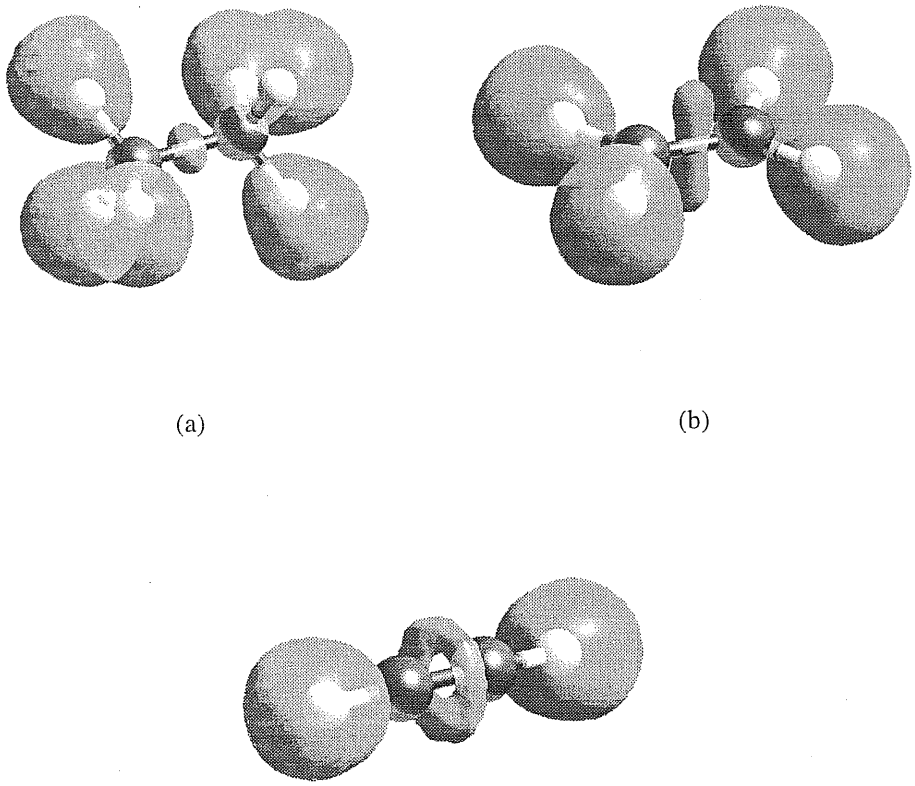

Figure 1.2: ELF three–dimensional isosurfaces with ELF=0.85: (a) ethane, (b) ethylene, and (c) acetylene. In the ball–and–stick models black and white balls represent, respectively, carbon and hydrogen atoms.

1.2.3 Bulk crystals: metallicity vs. covalency

Detailed ELF analyses have been performed for many systems of chemical interest [4–7]. In a bulk crystal, the most relevant performance of ELF is undoubtely the ability to sharply discriminate between metallic and covalent bonding. This is illustrated in the left panels of Figs. 1.3 and 1.4, where we plot the ELF for two paradigmatic crystalline materials: respectively, silicon and aluminum.

Since the early days of electronic–structure theory, we understand bonding in simple metals through the paradigm of pseudopotential perturbation theory [23, 24]: the valence electrons behave basically as a free–electron gas in the region outside the ionic cores. At the opposite extreme, we understand covalent bonding through the paradigm of the H_2 molecule, whose electrons are strongly paired in a singlet state; in a more general case, covalent bond is characterized by "localization" of valence–electron pairs in appropriate regions of space. While charge–density plots do not help much in discriminating metallic from covalent, the ELF provides a quantitative measure of "metallicity" vs. "covalency" of a given bond, or more generally of a given valence region of the system.

Si Bulk

In the bulk silicon, one clearly sees the almost black regions in Fig. 1.3 between nearest–neighbor atoms, whose bonding pattern in this geometry has the shape of a "zig–zag"chain. In these bonding regions our calculated ELF attains the maximum value of 0.96, thus indicating that the Pauli principle has little effect. In agreement with a chemical picture of the covalent bond, we associate these regions to the opposite–spin electron pairs—actually a "bosonic" system—localized between every pair of bonded atoms. This is to be contrasted to metallic bonding, where the valence electrons have a free–electron nature. To make this point better

Al Bulk

clear, we take as an example a paradigmatic simple metal: crystalline aluminum, whose bulk ELF is shown in the left panel of Fig. 1.4 to the same grey scale. Comparing this plot with that one of silicon in Fig. 1.3 we immediately appreciate the spectacular ELF ability to distinguish in a very clearcut way between metallic bonding and covalent bonding. The ELF plot in aluminum shows—outside the core regions—a large grey area, which correspond to a jellium–like (or Thomas–Fermi) ELF value. Actually, the maximum value attained by ELF between nearest—neighbor atoms is only 0.61 and—outside the core radii—there is a widespread grey region, where ELF is almost constant and close to 0.5, thus indicating the free–electron nature of the valence electrons. The ions cores only provide an "exclusion region" for electrons (white circles in the plots), but basically do not alter this jellium–like electron distribution: in this sense, we may regard the ion cores as a "weak" perturbation [24].

Comparison of the two ELF plots provides therefore the most significant and perspicuous visualization of the important *qualitative* difference between the co-

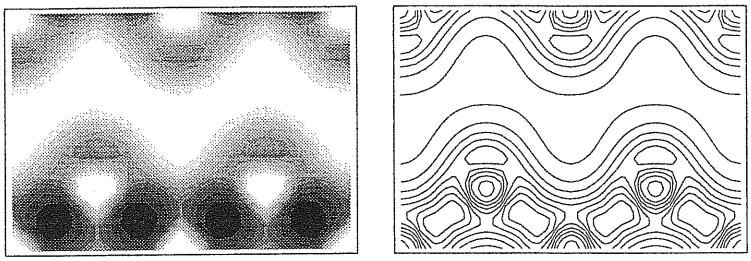

Figure 1.3: Contour plots for bulk silicon in the [110] crystalline plane. Left panel: ELF; right panel: pseudocharge density.

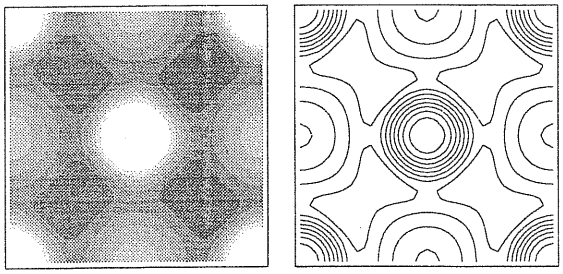

Figure 1.4: Contour plots for bulk aluminum in the [100] crystalline plane. Left panel: ELF; right panel: pseudocharge density. The same scale is used as in plot of Fig. 1.1.

valent bond and the metallic one. In the bulk of the two materials the Pauli principle plays quite a different role. The other typical tools for analysis, such as charge–density plots or projected density of states, lack by far a similar sharpness. As an example, we show the corresponding pseudocharge density plots in the right panels of Fig. 1.3 (silicon) and in Fig. 1.4 (aluminum). From such figures, hardly any information about metallicity or covalency can be drawn.

1.3 Bond polarity

ELF is a tool naturally devoted to the qualitative study of ionicity effects upon the bonding character. We report in Fig. 1.5 our results for a group of covalent systems and the limiting cases of an ionic compound.

For the zincblende semiconductors in Fig. 1.5, ordered with increasing Phillips ionicity [25], we have observed effects analogous to those cited in Ref. [7] for similar structures. The region of high ELF value becomes increasingly asymmetric

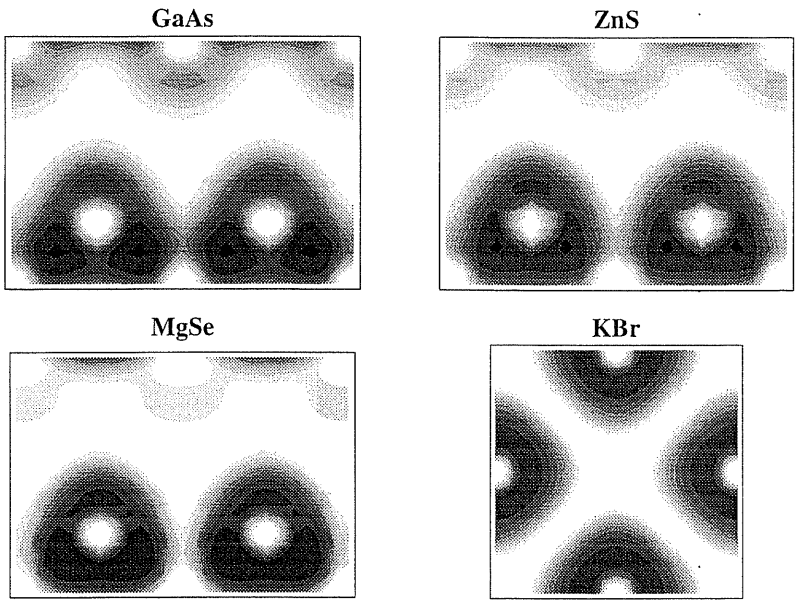

Figure 1.5: Contour plots of ELF in the [110] plane for different zincblende structures, ordered with increasing bond ionicity (GaAs, ZnS, MgSe) and an ionic compound (KBr).

and extended, with a clear tendency to concentrate around the more electronegative atom. In agreement with Ref. [7], we have also found a good correlation between the ratio of covalent radii and the distance of the ELF maxima from the relative nuclei.

The ionic crystal KBr is simply the limiting case of the zincblende sequence, with each Br atom surrounded by a nearly spherical cloud of high ELF value, corresponding to the filled valence shell. As expected the ELF topology in the ionic case is equivalent, for the Br atom, to the isolated–atom case in Fig. 1.1, with the complete valence shell localized around the nucleus.

It is important to stress also how the ELF is dimensionless, allowing to compare the nature of the chemical bond in different compounds, as the ones in Fig. 1.5, on an absolute scale. Only within an ELF approach it is possible to describe the ionicity effects in the bonding regions.

Chapter 2

N-representability, Equidensity Orbitals, and ELF

In this chapter we provide a novel solution of the N-representability problem for an extended system, which implies an explicit form for the Kohn–Sham kinetic energy in terms of the density. Our approach is based on a periodic coordinate mapping, which transforms a reference uniform system into the actual nonuniform one. The kinetic energy density functional is thus expressed as an explicit functional of the metric tensor. Since N-representability is enforced, our constructive recipe provides a variational approximation. Furthermore, we show that our geometric viewpoint is quite naturally related to the ELF which—as obtained from accurate Kohn–Sham orbitals in real materials—allow an appraisal of the variational approximate kinetic energy density functional.

2.1 The N-representability problem

The celebrated basic tenet of density–functional theory [16, 18–20] states that an exact description of a many–electron system is in principle possible in terms of a single scalar field, namely the electron density $n(\mathbf{r})$. The Hohenberg–Kohn theorem [18] (upon which DFT is based) does not provide a constructive scheme: for any given N, the *exact* functional is indeed accessible only through the many–body wavefunction.

The enormous success of DFT resides in *approximate* schemes which are constructive, and do not make explicit recourse to the many–body wavefunction:

within such schemes, the only wavefunction needed is a wavefunction of non-interacting electrons, which is uniquely defined by the manifold of the occupied Kohn–Sham single–particle orbitals [16, 19, 20], or equivalently by the KS one–body reduced density matrix. The eponymous density functional $F[n]$, Eq. (2.18) below, is the sum of a few terms: all of them but one are almost invariably approximated as explicit functionals of the density. The only term where the density matrix is actually needed is $T_{\rm s}$, the kinetic energy of the noninteracting system, which is a functional of the density in an implicit way. This qualitative difference is of course responsible for most of the computer workload in practical calculations, hindering amongst other things the linear scaling of computations with the size of the system.

A well known approximate form for the kinetic energy of a system of noninteracting electrons in terms of their density is the Thomas–Fermi (TF) one [26]. We focus here on a different class of approximations, which are—at variance with TF—variational: this feature is intimately linked to the problem of N-representability, which concerns the reconstruction of the antisymmetric many–body wavefunction generating a given density. In fact, even if one can easily construct an entire family of antysimmetric N-electron wavefunctions corresponding to a given reasonable density, the energy associated to this trial wavefunctions is far from being the true ground–state energy, even in the simple case of non interacting electrons. This happens because fixing the density is not sufficient to restrict the Hilbert space to an "acceptable" subset of many–body wavefunctions and a very special attention must be paid to the kinetic energy.

Whenever an approximate $T_{\rm s}$ coincides with the true kinetic energy of an arbitrary independent–electron wavefunction, then the variational theorem ensures that it must be no smaller that the exact $T_{\rm s}$ of the given system. Therefore, the requisite of N-representability is equivalent to requiring that $T_{\rm s}$ obtains from a density matrix which is idempotent. There is clearly an infinity of idempotent density matrices, all yielding the same given density: amongst these infinite solutions of the N-representability problem, one searches for the one having the lowest $T_{\rm s}$ at the given density.

In order to provide an explicit approximate (and variational) expression for $T_{\rm s}$ one has, first of all, to provide a constructive recipe which, starting from a given

density, produces an idempotent density matrix. Explicit solutions of this problem have been provided by several authors in the literature, amongst whom we only quote Harriman [27], Zumbach and Maschke [28], and Ludeña and coworkers [29–31]. The solution proposed by Harriman—for the one–dimensional case—can be simply summarized in the following.

Harriman construction

Given a one–dimensional N electron system at density $n(r)$, with

$$\int_{-\infty}^{\infty} dr\ n(r) = N, \tag{2.1}$$

one defines an auxiliary function $f(x)$ by the differential equation

$$\frac{df(r)}{dr} = \frac{2\pi}{N} n(r). \tag{2.2}$$

Direct integration of Eq. (2.2) yields:

$$f(r) = \frac{2\pi}{N} \int_{-\infty}^{r} dt\ n(t). \tag{2.3}$$

A constructive solution to the N-representability problem is achieved by the determination of an idempotent density matrix whose trace yields the given charge density. Starting from the condition (2.2) imposed on the auxiliary function $f(x)$, Harriman proposed the following set of single–particle orbitals $\phi_k(r)$ labelled by an integer "quantum number" k:

$$\phi_k(r) = \sqrt{\frac{n(r)}{N}} e^{ikf(r)}, \quad k \in \mathbb{Z}. \tag{2.4}$$

Notice that the orbitals $\phi_k(r)$ have a k–independent density, and are therefore "equidensity orbitals" in Harriman's [27] nomenclature.

By means of Eq. (2.2) one readily demonstrates that these orbitals are orthonormal:

$$\begin{aligned} \int_{-\infty}^{\infty} dr \phi_l^*(r)\phi_k(r) &= \int_{-\infty}^{\infty} dr \frac{n(r)}{N} e^{i(k-l)f(r)} \\ &= \frac{1}{2\pi} \int_{-\infty}^{\infty} dr e^{i(k-l)f(r)} \frac{df(r)}{dr} \\ &= \frac{1}{2\pi} \int_{0}^{2\pi} df e^{2\pi i(k-l)f} = \delta_{kl}, \end{aligned} \tag{2.5}$$

and complete (provided $n(r)$ does not vanish on a set of finite measure, so that $f(r)$ is a strictly monotonically increasing function):

$$\begin{aligned}\sum_{k\in\mathbb{Z}} \phi_k(r)\phi_k^*(r') &= \frac{1}{N}\sqrt{n(r)n(r')}\sum_{k\in\mathbb{Z}} e^{2\pi i k[f(r)-f(r')]} \\ &= \frac{2\pi}{N}\sqrt{n(r)n(r')}\delta(f(r)-f(r')) \\ &= \frac{2\pi}{N}n(r)\frac{\delta(r-r')}{|df(r)/dr|} = \delta(r-r'). \end{aligned} \tag{2.6}$$

Thus the Slater determinants

$$D(k_1,\ldots,k_N) = \frac{1}{\sqrt{N!}}\det\{\phi_{k_1},\ldots,\phi_{k_N}\} \tag{2.7}$$

with $k_1,\ldots,k_N \in \mathbb{Z}$, and $k_i \neq k_j$ for $i \neq j$ constitute a complete orthonormal system of N-particle wavefunctions, each of which has a density identical with the prescribed function $n(r)$.

Zumbach and Maschke construction

An analogous construction in three dimensions [28] is based on the orbitals:

$$\phi_{\mathbf{k}}(\mathbf{r}) = \sqrt{\frac{n(\mathbf{r})}{N}}e^{\mathbf{k}\cdot\mathbf{f}(\mathbf{r})+\phi(\mathbf{r})}, \quad \mathbf{k}\in\mathbb{Z}^3. \tag{2.8}$$

In contrast to the one–dimensional case, where the condition (2.2) determines univocally $f(r)$, the corresponding requirement for the Jacobian in three dimensions leaves considerable freedom in the construction of the vector $\mathbf{f}(\mathbf{r})$. Zumbach and Maschke [28] have proposed a possible choice, and—once contructed the single–determinant many–body wavefunction $D(\mathbf{k}_1,\ldots,\mathbf{k}_N)$—have variationally fixed the phase factor $\phi(\mathbf{r})$, by minimizing the kinetic energy of a system of noninteracting particles.

Within our geometrical approach it is possible to gauge the quality of the equidensity orbitals set by simply looking at the ELF plot

Starting from a rather different viewpoint, we have proposed [11] an elegant generalization to extended systems of the Zumbach and Maschke construction: namely, we solve the N-representability problem for a system of N noninteracting electrons in a box of volume V, where periodic (Born-von Kàrmàn) conditions are assumed at the boundary. Basically, with a simple geometrical approach—in the same spirit as the one advocated by Gygi [32,33] in electronic structure calculations—we introduce an orthonormal and complete set of equidensity orbitals, analogous to that in Eq. (2.8), that formally solve the N-representability

problem. Moreover, our geometric description naturally partitions T_s into the sum of two terms: very roughly speaking "bosonic" and "Pauli". These two terms coincide with the volume integrals of the two local functions which are used in the literature as the main ingredients of the ELF: therefore our solution of the N-representability problem—as well as the explicit approximate density functional based upon such solution—is therefore fundamentally linked in a very natural way to the ELF concept. In particular, the ELF results shown in the first chapter for real materials help understanding what is good and what is bad in the approximate form of T_s. Anticipating here our result, we find that the quality of the approximation provided by our constructive recipe strongly depends on the kind of bonding involved in the many–electron system. We give evidence that both the Zumbach and Maschke recipe [28] and our own one provide a reasonable set of single–particle orbitals for simple metals in the pseudopotential approximation, while their quality significantly decrease whenever covalent bonding is present.

2.2 Curvilinear coordinates and N-representability

For a system of independent electrons in a closed–shell configuration the wavefunction is a single determinant: knowledge of the one–particle reduced density matrix is equivalent to a complete knowledge of the wavefunction. The spin–integrated matrix $\rho(\mathbf{r},\mathbf{r}')$ is twice a projector, which indeed projects over the (doubly occupied) one–particle orbitals. We consider a system of N electrons in a box of volume V, obeying periodic boundary conditions. The average density is $n_0 = N/V$, the density is $n(\mathbf{r}) = \rho(\mathbf{r},\mathbf{r})$, and the idempotency condition is written:

$$\int_V d\mathbf{r}''\, \rho(\mathbf{r},\mathbf{r}'')\rho(\mathbf{r}'',\mathbf{r}') = 2\,\rho(\mathbf{r},\mathbf{r}'). \tag{2.9}$$

Homogeneous system

We start with a homogeneous system of N non–interacting electrons at the same density n_0, for which we use $\boldsymbol{\xi}$ as a space coordinate. For this system the canonical orbitals are, by symmetry, the plane waves $e^{i\mathbf{k}_l\boldsymbol{\xi}}/\sqrt{V}$, where $\mathbf{k}_l$ are the reciprocal vectors determined by the boundary conditions. By choosing to occupy

the $N/2$ orbitals of lowest energy, the density matrix is:

$$\rho_0(\boldsymbol{\xi},\boldsymbol{\xi}') = \frac{2}{V}\sum_{l=1}^{N/2} \mathrm{e}^{i\mathbf{k}_l(\boldsymbol{\xi}-\boldsymbol{\xi}')}, \tag{2.10}$$

which is obviously idempotent and yields a constant density. In the thermodynamic limit ($N \to \infty$ and $V \to \infty$ at constant n_0) the $\mathbf{k}_l$ set becomes dense. Occupying the $\mathbf{k}$-vectors within the Fermi sphere ($|\mathrm{k}| < k_\mathrm{F}$) Eq. (2.10) yields the well known electron–gas result:

$$\rho_0(\boldsymbol{\xi},\boldsymbol{\xi}') = n_0 \frac{3j_1(k_\mathrm{F}|\boldsymbol{\xi}-\boldsymbol{\xi}'|)}{k_\mathrm{F}|\boldsymbol{\xi}-\boldsymbol{\xi}'|}. \tag{2.11}$$

Coordinate mapping

At this point we introduce a generic curvilinear coordinate precisely of the same kind as introduced by Gygi in the field of electronic–structure calculations [32, 33]. We therefore define a twice differentiable invertible map $\boldsymbol{\xi} \to \mathbf{r}(\boldsymbol{\xi})$, periodic over V, whose Riemannian metric tensor is:

$$g_{ij} = \frac{\partial r^k}{\partial \xi^i}\frac{\partial r^k}{\partial \xi^j}. \tag{2.12}$$

Summation over repeated indices is understood throughout. A generic plane wave of momentum $\mathbf{k}$ is transformed as:

$$\frac{1}{\sqrt{V}}\mathrm{e}^{i\mathbf{k}\boldsymbol{\xi}} \longrightarrow \chi_\mathbf{k}(\mathbf{r}) = \frac{1}{\sqrt{V}} g^{-\frac{1}{4}}(\mathbf{r})\mathrm{e}^{i\mathbf{k}\boldsymbol{\xi}(\mathbf{r})}, \tag{2.13}$$

where $g = \det\{g_{ij}\}$, and $g^{-\frac{1}{2}}$ is the Jacobian $|\partial\boldsymbol{\xi}/\partial\mathbf{r}|$ of the inverse transformation. The orbitals $\chi_\mathbf{k}(\mathbf{r})$, having a $\mathbf{k}$-independent density, are therefore a three–dimensional generalization of the Harriman's equidensity orbitals in Eq. (2.4).

The density matrix in the new coordinates is:

$$\begin{aligned} \rho(\mathbf{r},\mathbf{r}') &= \rho_0(\boldsymbol{\xi}(\mathbf{r}),\boldsymbol{\xi}(\mathbf{r}')) = \\ &= \frac{2}{V} g^{-\frac{1}{4}}(\mathbf{r}) g^{-\frac{1}{4}}(\mathbf{r}') \sum_{l=1}^{N/2} \mathrm{e}^{i\mathbf{k}_l[\boldsymbol{\xi}(\mathbf{r})-\boldsymbol{\xi}(\mathbf{r}')]}. \end{aligned} \tag{2.14}$$

The corresponding transformed density is

$$n(\mathbf{r}) = n_0\, g^{-\frac{1}{2}}(\mathbf{r}). \tag{2.15}$$

In the novel coordinates we thus have a nonhomogeneous system, with the same average density as the homogeneous one, and whose density matrix is idempotent by construction.

We are now ready to attribute physical content to the above mathematics. Suppose that the density $n(\mathbf{r})$ of an electronic system is given. We then look for a coordinate transformation $\boldsymbol{\xi} \longrightarrow \mathbf{r}(\boldsymbol{\xi})$ which maps the uniform density into the given density: a necessary and sufficient condition is Eq. (2.15). The solution is nonunique, since several different maps share the same Jacobian $g^{-\frac{1}{2}}$: we will argue below about an optimal solution, using a variationally adaptive metric in the sense of Gygi [32, 33]. Replacement into Eq. (2.14) yields the explicit form:

Solution to the N-representability problem

$$\rho(\mathbf{r},\mathbf{r}') = \frac{2}{N} n^{\frac{1}{2}}(\mathbf{r}) n^{\frac{1}{2}}(\mathbf{r}') \sum_{l=1}^{N/2} \mathrm{e}^{i\mathbf{k}_l[\boldsymbol{\xi}(\mathbf{r})-\boldsymbol{\xi}(\mathbf{r}')]}. \tag{2.16}$$

In one dimension the solution of Eq. (2.15) is unique, and we get here the periodic analogue of the Harriman construction [27]. In three dimensions, our result is related to the work of Zumbach and Maschke [28], the differences being that we deal with periodic systems, and we provide a more general explicit construction. A coordinate mapping, similar in spirit to the present one (and called "local scaling transformation"), has been previously introduced by Ludeña and coworkers for spherical atoms [30].

2.3 Density functional

The energy of the electronic system in the external potential v_{ext} is written, within DFT, as [16, 20]:

$$E[n] = \int_V d\mathbf{r}\, n(\mathbf{r}) v_{\mathrm{ext}}(\mathbf{r}) + F[n]; \tag{2.17}$$

$$F[n] = T_{\mathrm{s}}[n] + \frac{1}{2}\int_V d\mathbf{r} \int d\mathbf{r}' \frac{n(\mathbf{r})n(\mathbf{r}')}{|\mathbf{r}-\mathbf{r}'|} + E_{\mathrm{xc}}[n], \tag{2.18}$$

where atomic Hartree units have been used. As already anticipated, basically all the available constructive approximations to DFT provide E_{xc} as an explicit functional of the density $n(\mathbf{r})$, while instead the kinetic energy term T_{s} is:

$$T_{\mathrm{s}} = \frac{1}{2}\int_V d\mathbf{r}\, \nabla_{\mathbf{r}} \nabla_{\mathbf{r}'} \rho(\mathbf{r},\mathbf{r}')\Big|_{\mathbf{r}=\mathbf{r}'}. \tag{2.19}$$

The ground electronic energy, Eq. (2.17), is therefore an explicit functional of the density matrix, which has to be minimized under the constraints of idempotency, Eq. (2.9), and electron number.

Density–only kinetic energy functional

Replacement of our ansatz density matrix, Eq. (2.16), in the above expressions provides an upper bound to the electronic energy, explicitly expressed solely in terms of the density and of the metric. The approximate kinetic energy is:

$$\tilde{T}_{\rm s} = \sum_{l=1}^{N/2} \int_V d\mathbf{r}\, |\nabla \chi_{\mathbf{k}_l}(\mathbf{r})|^2. \tag{2.20}$$

Using then Eq. (7) of Ref. [33], the expectation value of the kinetic energy over a $\chi_{\mathbf{k}}$ orbital is the sum of two positive terms:

$$\langle \chi_{\mathbf{k}} | T | \chi_{\mathbf{k}} \rangle = \frac{k_i k_j}{2V} \int_V d\boldsymbol{\xi}\, g^{ij} + \frac{1}{2V} \int_V d\boldsymbol{\xi}\, A_i g^{ij} A_j, \tag{2.21}$$

where the "gauge potential" is:

$$A_i = \frac{1}{4} \frac{\partial \ln g}{\partial \xi^i}. \tag{2.22}$$

After summing over the $N/2$ doubly occupied states, we get

$$\tilde{T}_{\rm s}[n] = \tilde{D}[n] + T_{\rm B}[n], \tag{2.23}$$

where the reason for the notations will be clear in a moment.

Using Eq. (2.15), we cast the gauge term as:

$$T_{\rm B}[n] = \frac{n_0}{32} \int_V d\mathbf{r}\, g^{-\frac{5}{2}}(\mathbf{r})\, |\nabla g(\mathbf{r})|^2 = \frac{1}{8} \int_V d\mathbf{r}\, \frac{|\nabla n(\mathbf{r})|^2}{n(\mathbf{r})}. \tag{2.24}$$

In the latter expression, we notice that the metric formally disappeares from the gauge term, which is indeed identical to the von Weizsäcker energy functional, appearing also in the definition of ELF, Eqs. (1.2) and (1.3). As already stressed in Chapter 1, this energy coincides with the kinetic energy of a system of non-interacting bosons in their ground–state, having the given density $n(\mathbf{r})$: with this specific meaning, we may refer to $T_{\rm B}$ as to the "bosonic" energy. Our expression for $\tilde{D}[n]$ as a function of the metric shall therefore be a variational approximation to the integral of the *true* excess Pauli energy density $D(\mathbf{r})$ of Eq. (1.3).

The sum over the occupied states in $\tilde{D}[n]$ is most easily evaluated if we assume a cubic box. If we define E_0 as the kinetic energy of the homogeneous system:

$$E_0 = \sum_{l=1}^{N/2} |\mathbf{k}_l|^2, \tag{2.25}$$

it is then easy to recast $\tilde{D}[n]$ as:

$$\tilde{D}[n] = \frac{E_0}{3V} \int_V d\dot{\mathbf{r}}\; g^{-\frac{1}{2}}\, \mathrm{tr}\{g^{ij}\}. \tag{2.26}$$

We further notice that in the thermodynamic limit one has:

$$E_0 = \frac{3}{10} N k_{\mathrm{F}}^2 = c_{\mathrm{F}} V n_0^{\frac{5}{3}}, \tag{2.27}$$

where $c_{\mathrm{F}} = \frac{3}{10}(3\pi^2)^{\frac{2}{3}}$.

Putting all the previous formulas together and approximating T_{s} in Eq. (2.18) with $\tilde{T}_{\mathrm{s}}$, we obtain an approximate $F[n]$ as an explicit functional of the density and of the metric tensor. Since the density—owing to Eq. (2.15)—is in turn a function of the metric tensor, we use the latter as the independent variable. Ultimately, the electronic energy of the system, Eq. (2.17), is a variational explicit functional of the metric tensor $g^{ij}(\mathbf{r})$. This functional can be regarded as the periodic analogue of the one of Zumbach and Maschke [28], expressed in more compact form in terms of a different variable. Furthermore the explicit occurrence of the periodic metric in the $\tilde{D}[n]$ term makes feasible an adaptive optimization of the metric. Upon closely following Gygi's approach [33], the Fourier coefficients of the periodic metric are the natural variational parameters of the problem.

In the trivial case $v_{\mathrm{ext}}(\mathbf{r}) = 0$ all of the kinetic energy is due to $\tilde{D}[n]$, since the density is constant and $T_{\mathrm{B}}[n]$ vanishes. Furthermore the metric is the identity and the approximate kinetic energy equals the exact one: $\tilde{T}_{\mathrm{s}}[n] = T_{\mathrm{s}}[n] = E_0$, Eq. (2.27). The approximate functional $F[n]$ coincides with the exact one, *including* its exchange–correlation term if the exact electron–gas data [34, 35] are used therein (as usual). This suggests that the approximate functional should work reasonably well for a system close enough to the electron gas, such as a simple metal within a pseudopotential scheme.

2.4 Connection with ELF

The experience gained in investigating the ELF in real materials helps understanding the meaning and the limits of the approximate density functional such as the Zumbach–Maschke [28] one, as well as of the generalization proposed here.

Variational approximation for the Pauli excess kinetic energy density

Our explicit ansatz of Eq. (2.16) leads to the Pauli excess energy $\tilde{D}[n]$ of Eq. (2.26). It is interesting to see the consequences for the ELF, since the ansatz clearly leads to replacing the Pauli excess energy density, $D(\mathbf{r})$ in Eq. (1.3), with

$$\tilde{D}(\mathbf{r}) = \frac{E_0}{3V}\, g^{-\frac{1}{2}}\, \mathrm{tr}\{g^{ij}\} = \frac{1}{3} c_{\mathrm{F}} n_0^{\frac{5}{3}} g^{-\frac{1}{2}}\, \mathrm{tr}\{g^{ij}\}, \tag{2.28}$$

where the thermodynamic limit, Eq. (2.27), has been used. Considering now the inequality

$$\frac{1}{3}\mathrm{tr}\{g^{ij}\} \geq [\det\{g^{ij}\}]^{\frac{1}{3}} = g^{-\frac{1}{3}} = \frac{n^{\frac{2}{3}}(\mathbf{r})}{n_0^{\frac{2}{3}}}, \tag{2.29}$$

we get for the approximate Pauli energy density the lower bound:

$$\tilde{D}(\mathbf{r}) \geq c_{\mathrm{F}}\, n^{\frac{5}{3}}(\mathbf{r}). \tag{2.30}$$

From Eqs. (2.30) and (2.23), we can argue that a single coordinate transformation satysfing (2.15), applied to the ground–state of an homogeneous system, gives a kinetic energy equal to its lower bosonic limit plus a term always greater than the jellium limit. The only way to gauge the quality of our single–determinant wavefunction is to understand how the true kinetic energy density deviates from its bosonic lower limit. The ELF is exactly a measure of this deviation, and comparing with the ELF definition, Eq. (1.2), one easily realizes that even the optimal choice of the metric tensor will unavoidably provide values of ELF which are smaller than 1/2 everywhere. From the ELF plots reported in Chapter 1, it is evident how in covalent or ionic systems—see, as paradigmatic examples, Figs. 1.3 and 1.5—the kinetic energy, particularly along the bonding direction, reaches its minimum (bosonic) value. The only systems where the kinetic energy is almost equal to its Thomas Fermi limit are the bulk metals, Fig. 1.4, where the coordinate mapping (2.15) should give a good approximation to the true ground–state many body wavefunction.

2.5 Conclusions and perspectives

With our work we have shown that a fundamental link exists between N-representability, approximate explicit functionals, and ELF. This link emerges very naturally within the geometric approach upon which our work is based. The same geometric approach, however, also indicates very clearly the limits of the approximate form of the kinetic energy for real materials which we have found here. In fact the final considerations of the previous paragraph imply that our constructive recipe, as well as the previous one of Zumbach and Maschke [28], are a good approximation only for systems where the bonding is metallic, while it necessarily overestimates the kinetic energy (and the total energy) whenever covalent bonding is present. Looking more closely, this major limitation owes to the occurrence of equidensity orbitals in our ansatz density matrix, Eq. (2.14), which occurrence can be further traced back to the choice of the uniform electron gas as the reference system upon which we perform the coordinate transformation.

This naturally suggests the directions for improvements: one should start from a reference model system other than the uniform electron gas, having instead some covalent bonding features already built in. Interestingly, the use of a model reference system designed to reproduce—after coordinate mapping—some desirable features of the real one has been proposed in the most recent work of Ludeña and coworkers [30, 31]. These authors, however, focus on a spherical atom having several electronic shells: here instead we are discussing a condensed system with only one valence shell, within a pseudopotential scheme.

Chapter 3

Crystal Surfaces

For every given solid surface, breaking of periodicity in one dimension will result in a change in the electronic states near and at the surface, since the lack of nearest neighbours on one side of the surface atoms causes a sensible local rearrangement of the surface structure and chemical bonds. From this point of view bonding at a crystal surface looks like an ideal arena for an ELF investigation, and we will show in the following how ELF—applied within a first–principles pseudopotential framework—provides an unprecedented insight into the surface bonding mechanisms.

In this chapter we consider two paradigmatic cases, corresponding to the two very different bonding characters perspicuously visualized via an ELF approach: namely, the covalent and the metallic bond.

We first consider the bonding pattern of a covalent semiconductor surface—the Si(001)—in its unreconstructed (truncated bulk) and reconstructed geometries. Finally, we investigate some surfaces of a paradigmatic sp bonded metal—namely, Al(110), Al(100), and Al(111)—where the ELF discriminates in a very sharp, quantitative, way between different kinds of bonding.

3.1 Semiconductor surfaces: the case of Si(001)

The driving mechanism for surface reconstructions of a covalent material is the tendency of low–coordinated surface atoms to saturate dangling bonds. It is then obvious that a completely different bonding pattern differentiates the unreconstructed (*i.e.* bulk terminated) surface from the reconstructed one. When several different reconstructions are compared, these show in turn different bonding features.

We present a state–of–the–art thorough investigation about a paradigmatic case: namely, the silicon (001) surface [12]. Although bonding at a crystal surface can be considered as a natural application for an ELF investigation, we are aware of only one work, which however is performed at the non–selfconsistent tight–binding level [36].

We show that the insight into the nature of bonding at the surface is very accurate and clear when the ELF is analyzed. We demonstrate—through a series of contour plots in high–symmetry planes—the outstanding ability of ELF in discriminating between the surface bonds occurring upon dimerizations at the Si(001) surface, thus providing an unprecedented insight into the physical mechanisms which drive the reconstruction. Dangling orbitals and surface bonds are visualized with a resolution incomparably sharper than by using the current tools, such as charge–density plots or projected densities of states.

Elemental systems: the key issue is metallic vs. covalent bonding

The case study chosen here is possibly the theoretically best known semiconductor surface. Its most relevant features are therefore very well understood in the literature: in particular, the unreconstructed surface is metallic and the reconstructed one is insulating [37]. The aim of the present approach is not to demonstrate anything at variance with the common wisdom. Instead, our aim is to show how the known features of this surface can be recovered in a simple and meaningful way from an ELF analysis. It is also worth to stress that the ELF *does not* make use of the spectrum of the system, while instead is a pure ground–state property.

3.1.1 Technical details

The (001) silicon surface is strongly reconstructed, with several different reconstructed structures. A relatively simple (2×1) reconstruction is formed by surface atoms moving together in pairs to form dimers.

The driving force for the dimer formation is the elimination of a dangling bond from the surface atoms. Each atom of the unreconstructed surface is bonded to only two neighbours and therefore has two dangling bonds projecting out of the surface. If the atoms move together in pairs, forming a new bond between them, then one of these dangling bonds will be eliminated from each member of the pair. This leads to a considerable energy gain since half of the broken surface

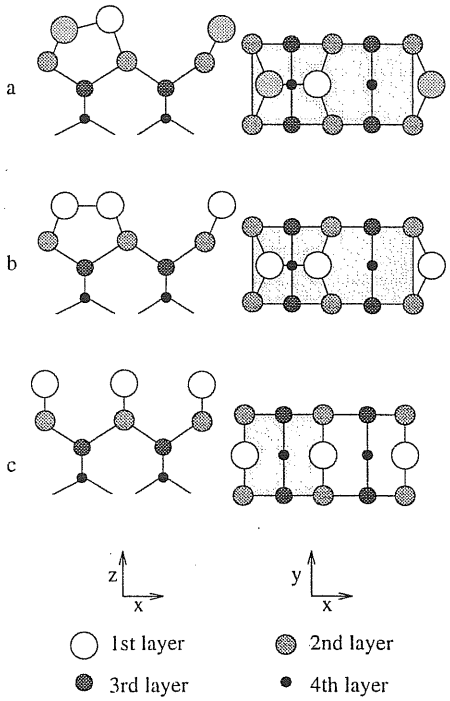

Figure 3.1: Side (left) and top (right) views of the (2×1) reconstructions of the Si(001) surface. (a) Buckled–dimer, (b) symmetric–dimer, and (c) ideal (bulk–terminated) surface. The atoms in the first four layers are shown, with symbols as indicated in the figure bottom. The surface unit cells (shaded areas) are also shown.

bonds are reconstructed. The buckled dimer model is a simple modification of the dimer model in which each dimer is tilted or "buckled" out of the plane of the surface. We have considered therefore the unreconstructed and the (2×1) symmetric and buckled dimer surfaces, in order to better understand the connection between surface reconstruction and electronic localization. A schematic side and top view of these three surfaces is shown in Fig. 3.1.

All the calculation use quite standard ingredients: a plane–wave expansion of the KS orbitals with a 10 Ry kinetic–energy cut–off, 16 **k**-points on a Monkhorst and Pack [38] mesh for the irreducible Brillouin zone integration, and a norm–conserving pseudopotential in fully non–local form [39]. All our calculations were performed in a supercell geometry where the surface is modeled by a finite–size slab periodically repeated in the direction normal to the surface. For the ideal (bulk terminated) surface we use a unit cell containing 11 layers of atoms separated by the equivalent of 13 atomic layers of vacuum. For the symmetric and

buckled dimer (2×1) surface, we have reproduced the Roberts and Needs [40] calculation, using directly their relaxed atomic coordinates.

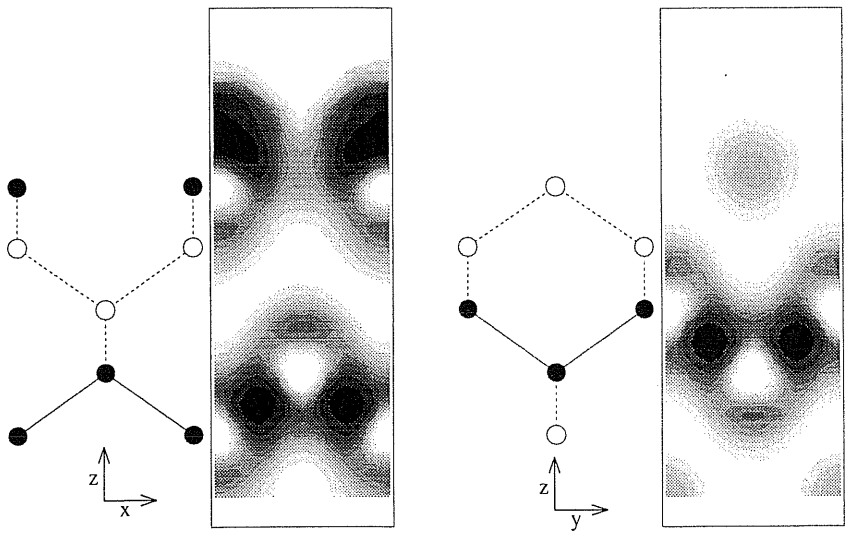

(a) (b)

Figure 3.2: ELF contour plots for Si(001) bulk terminated surface. (a) Plane orthogonal to the surface, containing two surface nearest–neighbor atoms: the relative dangling orbitals are revealed by the black ELF regions. (b) Plane orthogonal to the dangling bond, passing through the center of the surface unit cell: the fermionic channel between the two surface atom has a perfect circular symmetry. In the schematic side view, black balls and solid lines correspond, respectively, to in–plane atoms and bonds; white balls and dashed lines to off–plane atoms and bonds.

3.1.2 Results

We show in Figs. 3.2(a) and 3.2(b) the ELF contour plots for the unreconstructed surface along two non–equivalent planes orthogonal to the surface plane. First of all, looking at the bulk region in Fig. 3.2, and comparing to the crystalline silicon in Fig. 1.3 of chapter 1, we see how at only one atomic layer from the surface, the system has substantially recovered its bulk limit.

Bulk terminated surface

We now move to discuss the surface results. Focussing on the surface region in Fig. 3.2(a), one notices that the two dangling orbitals are very well visualized

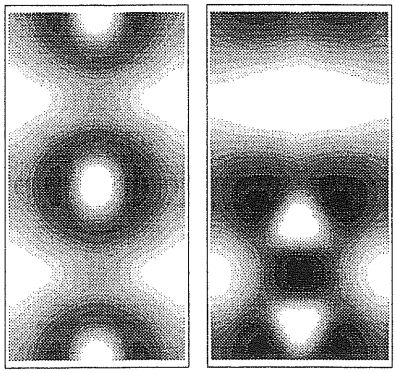

Figure 3.3: Si(001) bulk terminated (left panel) and symmetric–dimer reconstructed (right panel). ELF contour plots along surface plane passing through the topmost atoms.

by the ELF plot: every dangling bond is associated to an *isolated* electron, thus corresponding to an high ELF value. However, a more striking bonding feature of the same unreconstructed Si(001) surface is detected when analyzing ELF in the orthogonal plane, passing midway between two nearest neighbor surface atoms (Fig. 3.2(b)). There is a grey "fermionic channel"—defined as a region where ELF is of the order of 0.5—between the two nonbonded atoms: this channel in the midpoint has a perfect circular section, but it is actually formed by two grey–ELF strips going round the surface atoms and intersecting at the midpoint, as clearly shown by a top view (left panel of Fig. 3.3).

Reconstructed surface

The presence of this extended metallic–like system along the unrelaxed surface must be connected to the strong surface strain, due to the nonbonded atoms. As soon as the surface is relaxed and the dimer formation is allowed, there is a strong surface "bosonization", associated with a sizeable reduction of the fermionic channel. This localization effect due to the dimerization process is perspicuously shown in Fig. 3.3, where the unreconstructed situation is compared to the reconstructed one, for the symmetric–dimer case. The metallic character of the unreconstructed surface, and the insulating character of the reconstructed one, are well documented in the literature [37]. What is remarkable here is that ELF visualizes such characters without using *any* spectral information about the system.

Comparing the unreconstructed surface in Fig. 3.3 to the case of a bulk metal, as in Fig. 1.4 of chapter 1, we recognize, between the two neighbouring surface atoms, a "typical" metallic bond. Also the dangling orbitals, clearly correspond-

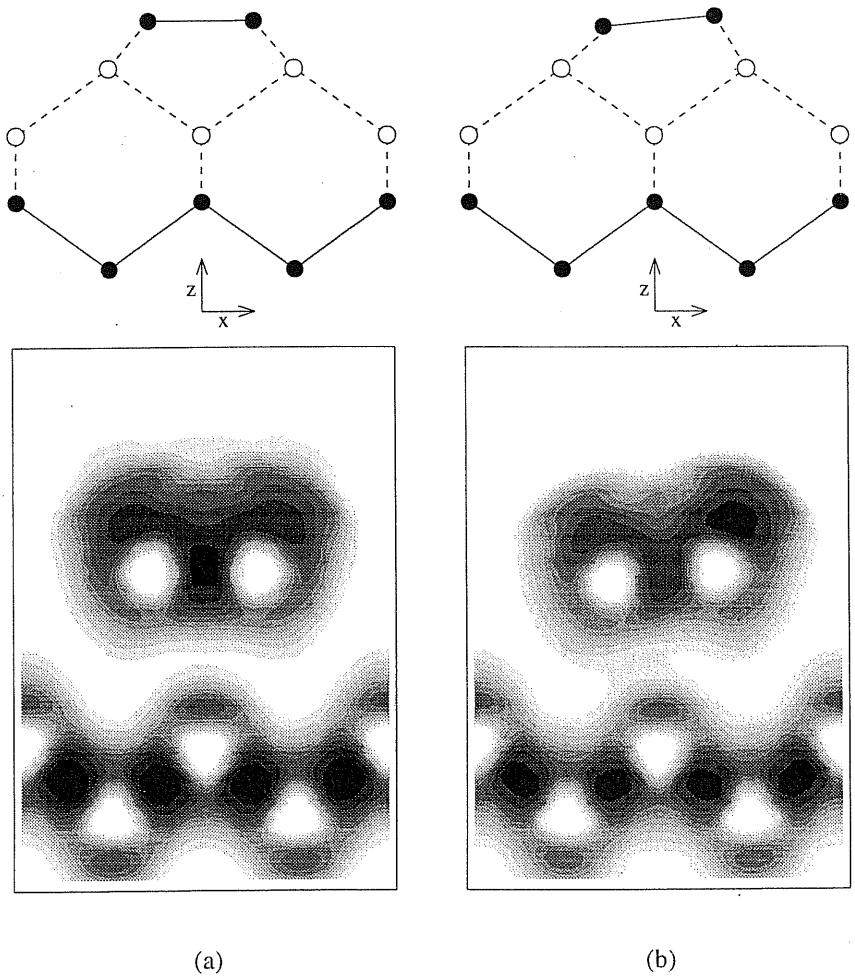

Figure 3.4: Si(001) (2×1) reconstructed surface: ELF contour plots along plane orthogonal to the surface, containing the dimer. (a) Symmetric–dimer surface and (b) buckled–dimer surface. For the schematic side view, symbols as in Fig. 3.2.

ing in Fig. 3.2(a) to strong localization regions—with an ELF maximum calculated along the direction passing through the surface atom and orthogonal to the surface plane equal to 0.9—are commonly associated to the non vanishing density of states observed in the gap [36, 37]. In other words the ELF sharply discriminates between two very different "metallic environments": the *singly–occupied* localized orbitals responsible for the states in the gap, and the purely metallic bond, where we observe a predominant Thomas–Fermi electron distribution. This is not surprising, since for the lone electrons lying in the *localized* dangling or-

bitals the Pauli principle is almost ineffective. On the contrary, a metallic bond is formed by occupation of a fully delocalized orbital where the electron strongly feels the effect of Pauli principle: therefore, its kinetic energy density sensibly deviates from its bosonic lower bound, yielding an almost jelliumlike ELF.

A more detailed analysis of the ELF variations induced by re–bonding at the surface is provided by Fig. 3.4(a) for the symmetric–dimer case and in Fig. 3.4(b) for the buckled–dimer one, both drawn in the plane passing through the surface atoms, and to be compared to the analogous plots of Fig. 3.2 for the unreconstructed case. In both cases the dimer has a strongly covalent bond character and is surrounded by a region of high ELF values: such localization effect is clearly connected to the surface reduced coordination, since the ELF around the isolated topmost atoms has a more pronounced atomic character.

3.2 Eletron localization at metal surfaces

We investigate here aluminum, which (as already stressed in Chapter 1) as a bulk material is a paradigmatic jelliumlike metal: cohesion and bonding are dominated by electron–gas features, where the ions can be considered roughly speaking as a perturbation. What happens at an Al surface, however, is much less intuitive: does the surface behave essentially like a jellium surface, or do surface atoms play a preminent role? Here we investigate this issue and we show how a sharp answer is provided by an ELF analysis.

Correlation between packing and bonding properties

We study here three basic choices for the orientation of the Al surface: (110), (100), and (111), schematically shown in Fig. 3.5. These high–symmetry surfaces have a rather different packing of the surface atoms: this is also visible in Fig. 3.5, where the same scale has been used for the three surfaces. Some correlation between packing and bonding properties is obviously expected, but what is surprising is that the three chosen surfaces span the whole range of possibilities, with (110) and (111) being at the two very extreme ends: while the Al(110) surface prominently displays well characterized Al atoms, Al(111) is essentially a weakly perturbed jellium surface. The atomiclike vs. jelliumlike character of the electron distribution is perspicuously shown by the immediate graphical language of ELF.

In a recent very interesting paper, Fall *et al.* [41] have investigated the trend in the Al work function for the same three orientations as considered here. They provide an explanation of the trend in terms of "face–dependent filling of the atomiclike p states at the surface". The ELF is an orbital–independent tool, yet it provides a concomitant message: we show that there is indeed a face–dependent filling of the electronic states localized in the surface region.

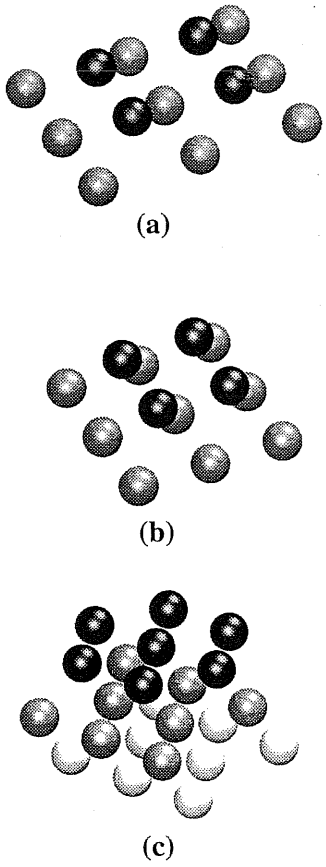

Figure 3.5: Schematic three–dimensional view of aluminum surfaces cut along different crystal orientations. (a) (110) surface, (b) (100) surface, and (c) (111) surface. Black balls correspond to topmost atoms, gray balls to second–layer atoms, and (for the (111) surface) white balls to third–layer atoms.

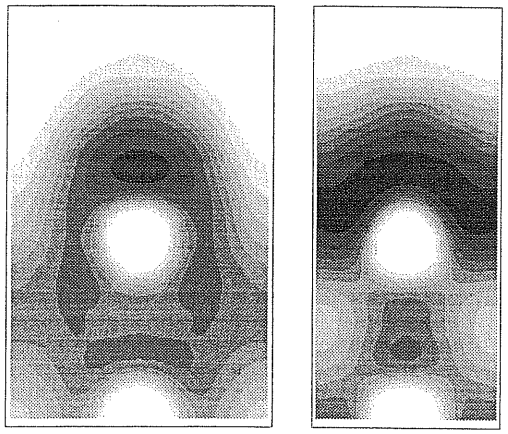

Figure 3.6: Al(110): ELF contour plot in two non–equivalent planes containing the topmost atom and orthogonal to the surface.

3.2.1 Geometry and calculation details

All the calculations in this work use a state–of–the–art set of ingredients: a plane–wave expansion of the KS orbitals with a 16 Ry kinetic–energy cut–off, a set of Monkhorst–Pack [38] special points for the Brillouin zone integration, with a Gaussian broadening of 0.01Ry and a norm–conserving pseudopotential in fully non–local form [39]. The calculations for the (111) surface were performed using

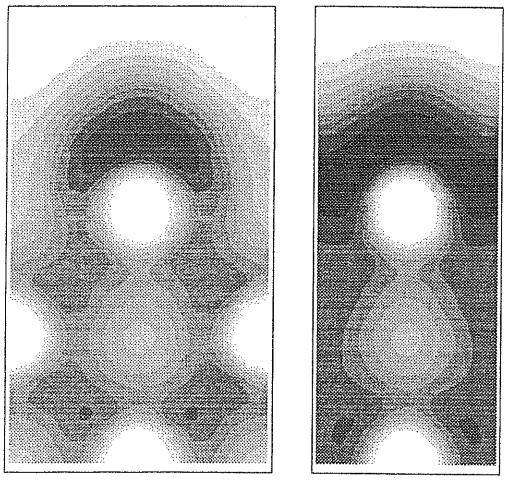

Figure 3.7: Al(100): ELF contour plot in two non–equivalent planes containing the topmost atom and orthogonal to the surface.

a 9+6 supercell (9 planes of Al, 6 equivalent planes of vacuum) and 37 **k**–points in the irreducible Brillouin zone. The corresponding values used for the (100) surface are an 8+6 supercell and 46 **k**–points, and for the (110) surface an 8+8 supercell and 48 **k**–points. We have preliminarily investigated the effect of surface ionic relaxation on ELF, and found it negligible. Similar insensitiveness was found in Ref. [41] upon other surface electronic properties: we therefore present results for the unrelaxed surfaces. As shown in Fig. 3.5, the three surfaces have a different packing: the packing increases from Al(110) to Al(100) to Al(111). A measure of this packing is the number of nearest neighbors in the surface plane, called coordination in the following: this number is 2, 4, and 6 for the three surfaces, respectively.

3.2.2 Results

Al(110)

In Fig. 3.6 we report two ELF contour plots along two non–equivalent planes passing through the topmost (twofold coordinated) atom of the Al(110) surface. Along a direction orthogonal to the surface and passing through the surface atom, our calculated ELF attains the maximum value of 0.89, thus indicating that the

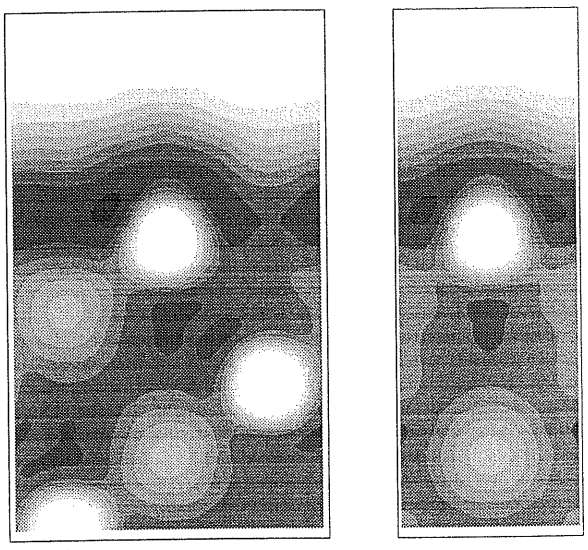

Figure 3.8: Al(111): ELF contour plot in two non–equivalent planes containing the topmost atom and orthogonal to the surface.

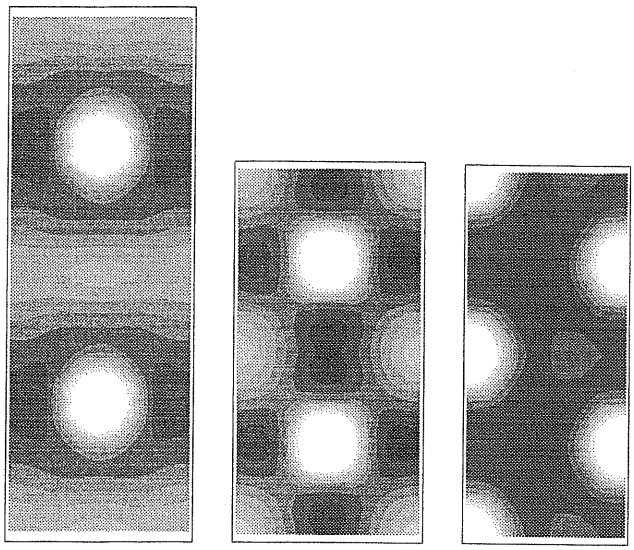

Figure 3.9: ELF contour plots in the plane containing the topmost Al atom for the three different orientations.

Pauli principle has little effect. Comparing Fig. 3.6 to Fig. 1.1, where the ELF maximum has the close value of 0.91, we quantitatively see see how much the surface atom actually behaves as a free–atom in the outer direction. A slightly Al(100) different electronic distribution is present at the four–fold coordinated Al(100) surface in Fig. 3.7. In this case the ELF maximum—along the same direction—attains the lower value of 0.80 and shows therefore an electron distribution with a less pronounced atomiclike character.

The almost black regions around the surface atoms in Figs. 3.6 and 3.7 are also clearly visible in the top views of Fig. 3.9, where the contour plots are drawn in the outermost atomic plane. In this plane the maxima occur midway between nearest-neighbors atoms and assume the values of 0.77, 0.74, and 0.67 in order of increasing packing. This decrease of electron pairing shows a trend from covalent–like to metallic–like bonding between nearest neighboring surface atoms; bonding to the underlying bulk atoms is instead metallic in all cases.

Finally, in Fig. 3.8 we have the extreme case of the six–fold coordinated Al(111) Al(111) surface. The absolute ELF maximum is only 0.73 and lies in a low–symmetry point, slightly off the outermost atomic plane. Along the direction orthogonal to the surface and passing through the surface atom, the ELF max-

imum is only 0.65: this behaviour clearly marks an almost smooth decay from the bulk—where the electrons exhibit a prevailing jelliumlike distribution—to the vacuum region. Also in the top view of Fig. 3.9 there is no evidence of electron pairing between surface atoms, with a wide spread region of almost uniform ELF, close in value to 0.5. We can therefore summarize the result by saying that the Al(111) surface is essentially a jellium surface perturbed by the atomic cores, in a pseudopotential sense [24]: the perturbation obviously originates an "exclusion region" (white plots within the core radii), but besides this has little effect on the electron distribution in the bulk *and* at the (111) surface.

The values of the maxima in the direction orthogonal to the surface and passing through the surface atom in the three cases (0.89, 0.80, and 0.65, as reported above) can be interpreted as a measure of the occupation of the atomiclike states protruding from the surface. We recall in fact that ELF is identically equal to 1 for any one– or two–electron system: high ELF values indicate a strong localization of the wavefunction. Our numbers show an analogous trend as the one pointed out by Ref. [41], where it is shown that the filling of atomic $p_\perp$ orbitals, protruding from the surface, decreases indeed with increasing packing, *i.e.* going from (110) to (100) to (111).

Chapter 4

ELF at Defects

The immediate graphical language of ELF can be proposed as a unique tool for investigating bonding in the presence of defects, either in crystals or in much more complicated systems, such as disordered clusters or amorphous materials. In both cases in fact there are over– or under–coordinated atoms, and often an unambiguous characterization of defects cannot be easily achieved by simply considering purely geometrical criteria. For these systems, the ELF yields therefore a meaningful real–space analysis of the bonding pattern, providing a first–principles characterization of all kinds of coordination defects.

In this chapter we first consider a perturbed bulk aluminum where we have substituted two atoms with "virtual" aluminum atoms, having a valence charge slightly different from the real one. The result that we obtain compares quite well with a first–order calculation on a perturbed jellium. Finally, we present our study of the coordination defects in amorphous silicon and hydrogenated amorphous silicon, also in their formation and their evolution upon hydrogenation. An accurate analysis of the valence charge distribution together with the ELF allows to resolve possible ambiguities in the bonding configuration, and in particular to identify clearly three–fold (T_3) and five–fold (T_5) coordinated defects.

4.1 Perturbed crystal aluminum

We have studied the effect of small charge fluctuations on the ELF. Specifically, we have considered a bulk virtual aluminum atom with a *small* core charge perturbation.

We have carried out this calculation in a supercell geometry (10 Al planes, 75 **k**–points, with 18 Ry energy cut–off), with two far aluminum atoms having,

respectively, a positive and a negative core charge fluctuation in order to preserve the overall charge neutrality. To restrict ourselves to the liner regime, we have chosen a small charge impurity by varying the core charge of 0.2 e. Given the predominant jellium–like character in the aluminum valence electronic distribution (see Fig. 1.4), we expect a strong similarity between the perturbed aluminum and an ideal jellium in the presence of a small localized charge fluctuation.

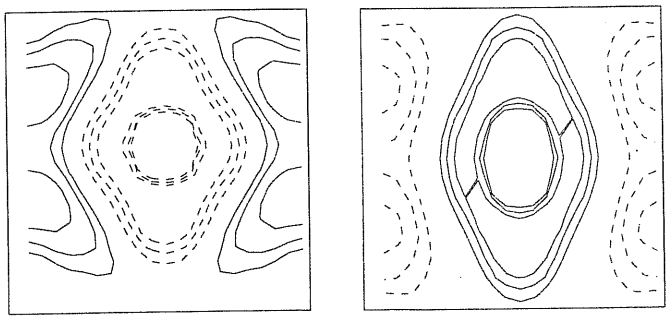

(a) (b)

Figure 4.1: ELF *differential* contour plots for bulk aluminum. Solid (dashed) isolines correspond to positive (negative) contours around zero. (a) Positive charge fluctuation; (b) negative charge fluctuation. ELF is visibly almost symmetric in the charge fluctuation: positive contour lines in (a) correspond to similarly–shaped negative ones in (b).

The results for the perturbed crystal aluminum are shown in Fig. 4.1: thanks to the linearity in the response, the ELF perturbations are almost equal in modulus and opposite in sign, yielding an odd function in the perturbation. This result is consistent with a first–order calculation performed on a jellium.

Considering a uniform system, and indicating with $\delta n(\mathbf{r})$ and $\delta T(\mathbf{r})$ respectively the charge and kinetic energy fluctuations in the presence of a small point–like perturbation, we have a non–vanishing first order term in the ELF written as:

$$\mathrm{ELF} = \frac{1}{2}\left(1 - \frac{\delta T(\mathbf{r})}{T_0} + \frac{5}{3}\frac{\delta n(\mathbf{r})}{n_0}\right). \tag{4.1}$$

The density and kinetic energy fluctuations $\delta n(\mathbf{r})$ and $\delta T(\mathbf{r})$ are linear functions of the external perturbation: therefore, from Eq. 4.1 the ELF of a perturbed jellium is a linear function of the perturbation.

4.2 Amorphous silicon: three–fold and five–fold coordination defects

Amorphous silicon (a-Si) and hydrogenated amorphous silicon (a-Si:H) are prototypes of disordered covalent semiconductors. Extensive work, both experimental and theoretical, has been done to study their topological and electronic structure. Although most of Si atoms are tetrahedrally coordinated, anomalously coordinated configurations can locally occur in pure and hydrogenated amorphous samples, but—at variance with the case of crystals where coordination defects can be easily recognized as deviations from the perfect ordered structure—their identification is not trivial. Hence, one of the most challenging problems in the amorphous systems is to localize the defects, to classify them and to identify their peculiar electronic features.

Traditionally, three–fold (T_3) defects have been considered as the most likely intrinsic defects in a-Si. The non vanishing density of states (DOS) observed in the gap has been commonly ascribed for a long time to the "dangling bonds" corresponding to these defects, and its lowering upon hydrogenation has been explained with the saturation of dangling bonds by hydrogen [42–49].

More recently, this picture has been debated and revised. In particular the importance of five–fold coordinated (T_5 or "floating bonds") in a-Si has been clearly stated in the theoretical works by Pantelides [50, 51] and Kelires and Tersoff [52] a some years ago, both in terms of their *existence* and their peculiar role in the electronic structure. The empirical simulation by Kelires and Tersoff has shown that T_5 atoms have lower energy than T_3 atoms, and therefore should be favoured in general. Also some *ab initio* molecular dynamics simulations of a-Si structures show a predominance of T_5 defects with respect to T_3 [53–55]. Pantelides [50, 51] argued that T_3 and T_5 are *conjugated defects* and must be considered on the same footing, since a bond elongation can transform a $T_5 + T_4$ structure into a $T_4 + T_3$ one, or vice versa an inward relaxation can transform a $T_4 + T_3$ structure into a $T_5 + T_4$ one; furthermore, he proposed a mechanism for H diffusion based on floating–bond switching and annihilation/formation of T_5's through interaction with H [51], which—at variance with the commonly accepted picture of dangling bonds hydrogenation—is compatible with the rapid decrease in the number of de-

fects without any appreciable change in the density of Si–H bonds experimentally observed at low temperature.

Some of these ideas have been widely used in discussing the *geometrical* characterization of defects; their soundness in terms of electronic properties has been investigated mainly by model calculations [43, 44, 56, 57] and more recently by some first–principles calculations [47, 49, 57, 58]. It remains the necessity of going beyond a pure geometric approach, with a simple tool that allow us to unambigously characterize the defects.

We focus in the present thesis on a real–space analysis of the bonding pattern of a-Si and a-Si:H using the simplest tools provided by first–principles electronic structure calculations: a comparative analysis of the electronic charge density and of the ELF [14]. We will show in the following how this approach yields a meaningful characterization of all possible coordination defects in silicon clusters.

4.2.1 Geometry and technical details

For studying the bonding properties in a-Si and a-Si:H we start from some selected samples generated by other authors [53–55] using Car–Parrinello first–principles molecular dynamics (CPMD)[1]. These structures reproduce quite well the experimental pair correlation function and bond angle distribution function using a reasonable number of atoms and hence they are suitable for accurate *ab initio* studies. The configurations studied are cubic supercells of side $a = 2\ a_0$, where a_0=10.17 a.u. is the theoretical equilibrium lattice parameter of c-Si, which also corresponds—in our calculations—to the optimized density of a-Si and a-Si:H. The supercells contain respectively 64 Si atoms to describe a-Si [53, 54] and 64 Si atoms plus 8 H atoms for a-Si:H [55].

We use state–of–the–art electronic structure methods based on DFT using norm–conserving pseudopotentials and plane–wave basis set [58]. The CPMD configurations, aiming mainly at reproducing the structural properties, have been obtained using a kinetic energy cutoff E_{cut}=12 Ry and the Γ point only for Brillouin Zone (BZ) sampling. We improve in our calculations the BZ sampling using 4 inequivalent special $\mathbf{k}$ points for self–consistency and 75 $\mathbf{k}$ points for DOS.

[1] A brief review of the Car–Parrinello approach is given in Appendix B.

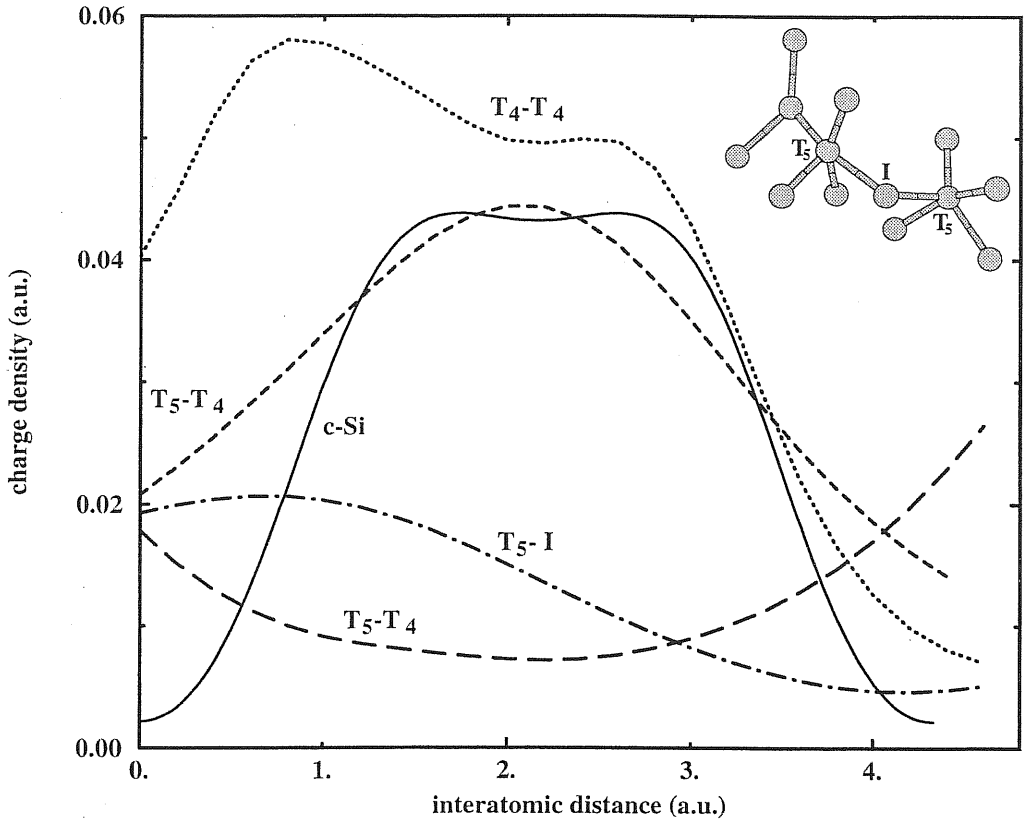

Figure 4.2: The inset shows a snapshot from the a-Si configuration including two T_5 defects with an intermediate four–fold coordinated atom (I) and other T_4 atoms (not individually labelled). For the intermediate four–fold coordinated atom we report, for clarity, only the two bonds connecting with the T_5 defects. The curves are the profile of the valence charge density along some bonds shown in the snapshot, connecting: two normally four–fold coordinated atoms (dotted line), a T_5 with a T_4 at "normal" distance (short–dashed line), a T_5 with a T_4 at "longer" distance (long–dashed line), a T_5 with I (dashed–dotted line). "Normal" and "longer" are with respect to the average bond length. For comparison also the perfect crystalline bond is shown (solid line). In order to filter out possible unrelevant local fluctuations, the charge distribution is filtered averaging over small spheres of radius R =0.6 a.u. moving along the bond. The distance is along the geometrical bond, calculated from one of the two atoms connected; note the different bond lengths. At variance with the crystalline case, the charge profiles are asymmetric with respect to the bond center, indicating a partially ionic character of the bond.

These parameters have been chosen as a reasonable compromise between accuracy and computational cost. The optimization of the a-Si and a-Si:H structures with the new computational parameters is accompanied only by small structural rearrangements, and therefore the mean structural properties are very similar to those reported by Buda *et al.* [53, 55] and Štich *et al.* [54] for the original con-

figurations. We only report that in a-Si the mean bond length is $d \simeq 4.47$ a.u., quite similar to the crystalline one which is 4.40 a.u.. The mean bond angle is $\vartheta \simeq 109°$, close to the characteristic value of the perfect tetrahedral network. The location of the first minimum of the radial distribution function defines geometrically the cutoff distance for the nearest neighbours (NN), which turns out to be $R_{NN} = 5.08$ a.u., giving an average coordination number of about 4.03. In a-Si:H the average Si–Si bond length is the same as in a-Si, but the first peak of the radial distribution function is more broadened and it is more appropriate to consider a larger NN cutoff distance, $R_{NN} = 5.49$ a.u.. Each H is bound to one Si atom with an average distance $d_{\mathrm{H}} = 2.95$ a.u., very close to the corresponding value in SiH_4 molecule.

4.2.2 Results

The standard *geometrical* analysis based simply on counting the atoms lying inside a sphere of radius R_{NN} indicates that the starting configurations have a predominance of T_5 defects and of distorted T_4 sites. Moreover, the a-Si computational samples do not contain well defined T_3 defects. This feature can be a consequence of the rapid quench from the liquid states which has been done in preparing the sample in the molecular dynamics process (since the liquid state is sixfold coordinated, a rapid quench typically favours over–coordination rather than under–coordination).

ELF for over–coordinated atoms

We start analyzing in detail an over–coordinated environment. For the sake of clarity, we will consider the case of a-Si (in a-Si:H overcoordination can be due to five Si neighbours, or to four Si and one H, and so on). In our a-Si sample there are two T_5 sites close one to each other (labelled A and B in the upper snapshot in Fig. 4.2), with a sort of interstitial (I) atom connecting them. A charge density analysis confirms for this configuration the bonding pattern predicted by the *geometrical* criteria, and helps in characterizing the different types of bonds [54]. We observe that T_5 sites are accompanied by a valence charge density depletion. The charge density profiles reported in Fig. 4.2 show in particular that some T_5–T_4 "long" bonds and the bonds T_5–I are characterized by a very small charge density; hence, they are "weak" and therefore those T_5 defects are the best candidates

to transform into T_3 sites after a bond elongation. The asymmetry in the bond charge profiles indicates that, at variance with the perfect crystalline environment, the bonds are not perfectly homopolar but have a certain degree of ionicity.

It is useful to compare this "standard" charge density analysis with the study of ELF. In the case of normal or floating bonds, the ELF does not add much more informations with respect to the standard charge density analysis. In the left upper panel of Fig. 4.3 we show the ELF=0.85 isosurfaces for the overcoordinated environment in a-Si described before. High–value charge density (not shown here) and ELF isosurfaces are almost similar in their extension and shape. The ELF isosurface in correspondence to the A–I bond clearly visualizes its bowing (the isosurface is not perfectly centered on the geometrical bond) and its weakness (the isosurface is smaller than those on the other bonds).

Adding two hydrogen atoms in the neigbourhood of the T_5 sites and allowing the system to relax, two Si–Si bonds are broken so that the atoms A and B become normally tetrahedrally coordinated, and their fifth NN atoms connect with the additional hydrogens (snapshot in the lower panel of Fig. 4.3). In this configuration all the Si–Si bonds are rather strong (the ELF isosurface between A and I is more extended with respect to the previous case) and more bulk–like (all the isosurfaces are more regular in shape). The plots of the density of states (right panels of Fig. 4.3) show that, at variance with the starting configuration having a metallic character evidently due to defect induced states in the gap, the final one is clearly semiconducting.

Dangling bonds are evidenced by ELF

The combined charge–density and ELF analysis is necessary to identify unambiguously the dangling bonds and to distinguish for instance a $T_5 + T_4$ configuration from a $T_4 + T_3$. Whereas the presence of a covalent bond is indicated by a region of local maxima of both ELF and charge density, a dangling bond is identified by a region with high values of ELF but low electronic charge density. This is evident in Fig. 4.4 (upper panels), where we show a snapshot from a a-Si:H sample with a T_4 (labelled A) and a T_3 (labelled B) atoms (we have created a dangling bond by removing an hydrogen initially bond to the silicon atom B). Panel (a) shows charge density isosurfaces, and panel (b) ELF isosurfaces. The absence of high–value charge density isosurface *together with* the presence of high–value ELF isosurfaces in the region between atoms A and B clearly indicate the pres-

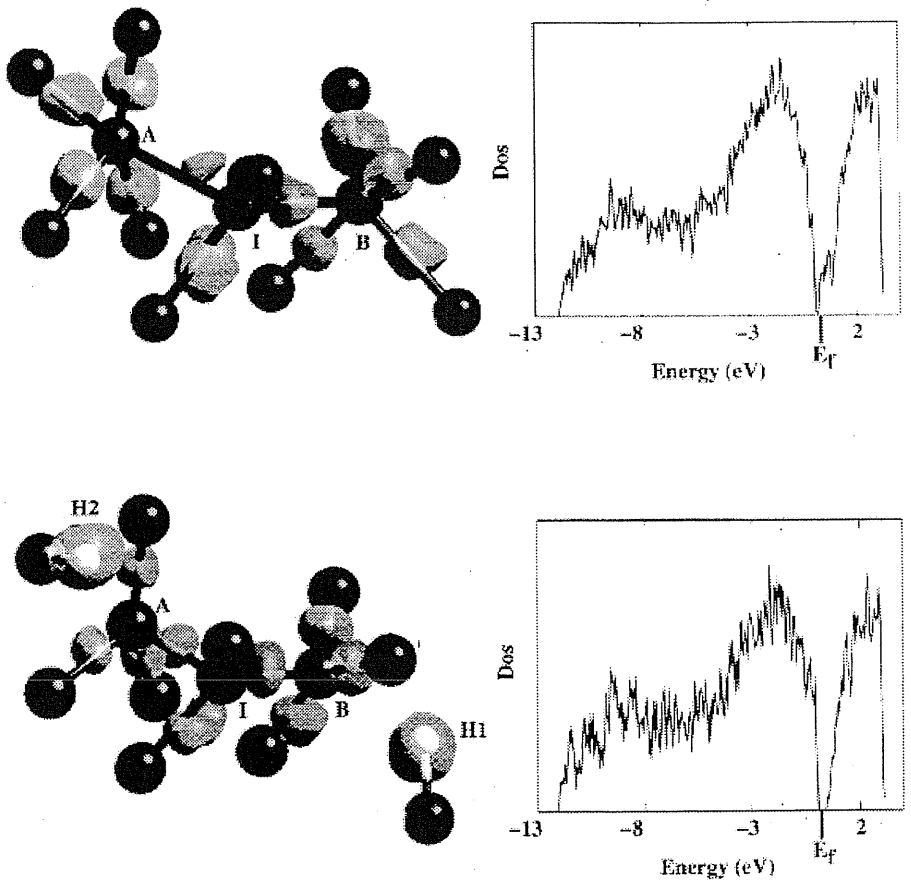

Figure 4.3: Upper panels: a snapshot from the starting a-Si configuration including two T_5 defects (A and B) with an intermediate T_4 atom (I). The ELF=0.85 isosurfaces are plotted: it is clearly visible the off–centered position and the small distorted shape between atoms A and I, indicating the bowing and the weakness of the bond. The total DOS of the a-Si sample is shown on the right, with electronic states close to the Fermi energy E_f. Lower panels: the structure evolved after addition of two H atoms (small white balls, H1 and H2) which have annihilated the T_5 defects. All the Si atoms of our sample are now "normal" T_4 sites, as shown by the more regular shape of the ELF isosurfaces and by the vanishing DOS in the gap.

ence of a dangling bond originated from atom B. As expected, this configurations has a metallic character, with electronic states around the Fermi energy E_f (panel (c) of Fig. 4.4).

When the system is allowed to relax, a new bond is formed between the silicon atoms A and B, as it clear from the panels (d) (charge density) and (e) (ELF). The final system has still gap states, both because of the T_5 defect B which is now formed and because other coordination defects are present in the rest of the a-

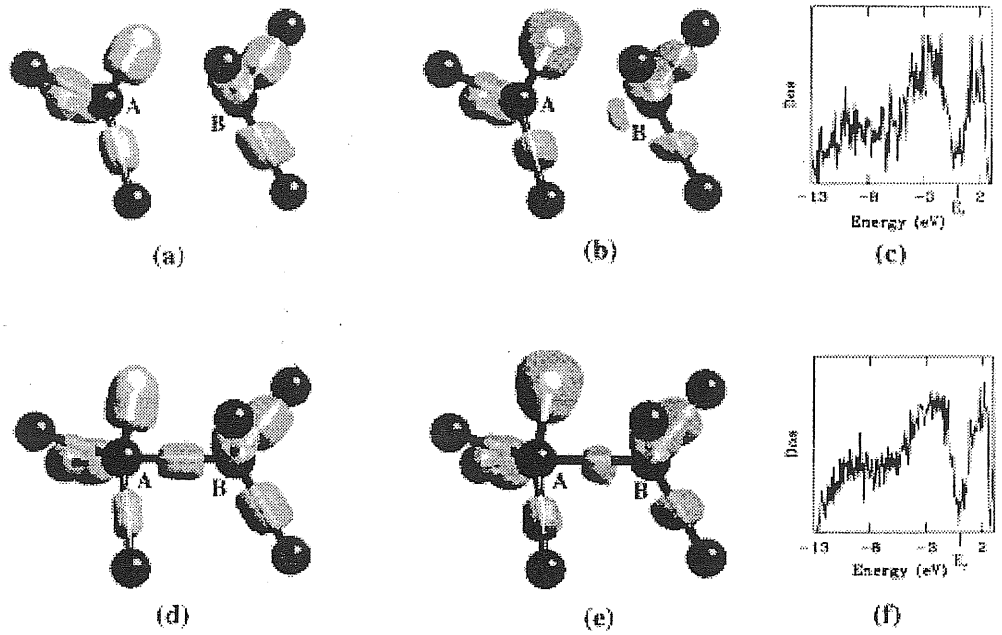

Figure 4.4: Upper panels: a snapshot from a-Si:H with a $T_4 + T_3$ structure (atom A and B respectively). Charge density isosurfaces (n=0.06 a.u.) and ELF=0.85 isosurfaces are plotted respectively in panels (a) and (b). The dangling bond on atom B is evident by comparison of the two plots as a region of low charge density but high ELF. The total DOS of the sample is reported in panel (c): the sizeable DOS around E_f is due to the T_3 defect and other defects in the sample. Lower panels: a snapshot containing the same atoms after relaxation, with a new bond formed between A and B atoms giving rise to a $T_5 + T_4$ structure. Charge density and ELF isosurfaces are plotted in panels (d) and (e) respectively, as in the previous case. The new A–B bond is characterized as a region of high charge density and ELF. The total DOS of the sample is reported in panel (f): gap states are still present.

Si:H sample. The evolution of this structure from a $T_4 + T_3$ into a $T_5 + T_4$ is consistent with the picture of Pantelides [50] of the conjugated T_3 and T_5 sites.

Part II

Enzymatic Catalysis from First Principles

Introduction

H-bonding is a key interaction for enzymatic structure, dynamics and catalytic functions, being responsible for the optimal substrate orientation and for the stabilization of the transition state.

In standard textbook descriptions of molecular interactions in enzymes, the H-bonds are normally classified as "weak" interactions, with an energy contribution usually estimated as large as 3 kcal/mol [59]. Anyhow, the recent observations [60–66] of unusually strong H-bonds in gas phase with an energy varying from 10 to 20 kcal/mol—characterized by peculiar NMR and IR signals, and low or vanishing barrier to proton transfer—have opened a new avenue for our understanding of biological catalysis. Indeed, enzymes could use the strong stabilization of this special class of H-bonds for their biological function.

Pauling [67] first suggested that an enzyme might be complementary to the transition state of a reaction and thereby speed up the reaction by binding the transition state and lowering the energy of activation along the reaction coordinate. Not only such a concept of complementary can help explain enzymes quantitatively, but also it provides a means of judging the quality of transition state analog inhibitors [68]. Nowadays, transition state complementary it is well established in all theories, and efforts are directed to understand the details of the complementary, whether it be electrostatic, particular bonding modes, or arrangement of molecules in the active site.

The observation of unusually strong H-bonds is supposed to give an interpretation to this complementary, and to finally explain the enzyme catalytic efficiency: namely, during the transition state formation, low–barrier (*i.e.* short, very strong) hydrogen bonds—in which the pK_a values of the proton donor and acceptor are matched—are postulated to contribute about 5 orders of magnitude to rate accel-

eration.

According to this new theory, the enzymatic mechanism is based on a conversion of a "normal" weak hydrogen bond (present in the enzyme–substrate complex) into a strong one by changing the pK_a value of the substrate, so that it is close to that of the enzymatic group to which it is hydrogen bonded.

A usual weak H-bond is essentially *electrostatic* in origin, and arises from the stabilizing interaction between the donor–hydrogen dipole and the dipole (or monopole) of the attractor atom [59]. As the overall donor–acceptor distance is reduced, and the proton affinities of the two atoms become similar, the H-bond transforms into a low–barrier H-bond: the bonding character is strongly *covalent* and an extra "resonance–stabilization" energy is released, due to the free hydrogen hopping between donor and acceptor.

The study of this very special class of H-bonds—uniquely characterized by the covalent bonding environment—can be considered as an ideal application field for an ELF investigation: as shown in the first part of this work, the ELF is an explicit measure for the degree of "covalency" of a given bonding region and its application to the analysis of the proton jumping occurring at low–barrier H-bonds sharply describes this kind of interactions [69–71].

In this thesis we provide a contribution in this direction, by analyzing the H-bond network present at the active site of serine proteases, an important and large class of enzymes catalyzing the cleavage of specific peptide bonds. The presence of a low–barrier H-bond between two conserved residues participating to the catalyzing action (His-57 and Asp-102), is revealed within an ELF approach in a rather simple and elegant way, shading new light onto the role of this kind of molecular interaction for the enzymatic process. Our finding, published in Ref. [69], is in complete agreement with a series of NMR experiments [66, 72–74] on enzyme–transition state analog complexes.

It is difficult to simulate low–barrier H-bonds with effective potentials, as the chemical bondsare continuously formed and broken. In contrast, low–barrier H-bonds are automatically described into an *ab initio* framework [75–81]. Indeed, the powerful combination of "standard" molecular dynamics simulation techniques with accurate density functional–based electronic structure calculations, makes feasible the study of the reactive processes in the presence of the

dynamical evolution of the environment. Also the temperature effects, playing a crucial role in a dynamical phenomena such as the low–barrier H-bond, are naturally included in this approach, having the unique ability to follow a given chemical reaction without any external adjustable parameter, or any other uncontrolled approximation.

These considerations make the method of choice for the present work—that is, *ab initio* molecular dynamics—a useful tool for the theoretical investigation of biological systems: in the last few years [82–85], the use of first principles molecular dynamics simulation has opened up a new and exciting research field, yielding a novel solution to long–standing problems in biochemistry.

Chapter 5

Proteolytic Enzymes

Enzymes are remarkable molecular devices that determine the pattern of chemical transformations. The most relevant features of enzymes are their catalytic power and specificity. Indeed, by utilizing the full repertoire of intermolecular forces, enzymes bring substrates together in an optimal orientation, to favor the making and breaking of chemical bonds. Upon substrate binding, they catalyze the reactions by stabilizing transition states, the highest–energy species in reaction pathways. By doing this selectively, an enzyme determines which one of several potential chemical reactions actually occurs.

The question of how enzymes greatly enhance the rate of reactions is central in biochemistry. The push and pull of electrons and the resulting bond changes are well understood for many enzymes. However, the larger question of general features that enzymes use to produce rate accelerations of 10^8–10^{15} has remained a contentious issue. Recently a new explanation for the "missing" transition state stabilization underlying the catalytic power of many enzymes has been suggested: under special conditions, a weak "normal" H-bond in the enzyme–substrate can become a "low–barrier" or short, strong H-bond. Formation of such a bond can contribute up to 20 kilocalories per mole to transition state stabilization.

A very important family of enzymes are the proteolytic enzymes (or proteases). These enzymes catalyze the cleavage of peptide bonds in other proteins. They are present in all forms of living organisms, having many physiological functions, ranging from generalized protein digestion to much more specific regulated processes.

In this chapter we briefly overview the main features of the enzymatic activity and the connection with the low–barrier H-bonds. Then we introduce the serine proteases, a family of proteolytic enzymes, whose detailed study is referred to a subsequent chapter.

5.1 Enzymatic activity

Catalytic power and specificity

Enzymes catalyze biochemical reactions by several orders of magnitude, as required by the cell metabolism. They are highly specific towards a given reactant, usually indicated as the *substrate*. An enzyme usually catalyzes a single chemical reaction or a set of closely related reactions. Side reactions leading to the wasteful formation of by–products rarely occur in enzyme–catalyzed reactions, in contrast with uncatalyzed ones.

An enzyme, as any catalyst, does not alter the *thermodynamical equilibrium* between reactants and products that would apply in its absence and it is rigenerated in its original form at the end of the reaction.

Enzymes accelerate reactions by stabilizing transition states

A chemical reaction of substrate S to form product P goes through a *transition state* $TS^{\ddagger}$ that has a higher free energy than either S or P:

$$S \rightleftharpoons TS^{\ddagger} \rightarrow P$$

The transition state is the most seldom occupied species along the reaction pathway because it has the highest free energy. The Gibbs free energy of activation $\Delta G^{\ddagger}$, is equal to the difference in free energy between the transition state and the substrate. With the symbols of Fig. 5.1

$$\Delta G^{\ddagger} = G_{TS^{\ddagger}} - G_{S}.$$

Enzymes accelerate reactions by decreasing $\Delta G^{\ddagger}$, the activation barrier of the reaction. Following the same symbols, in the presence of the enzyme E, the activation barrier changes as:

$$\Delta G^{\ddagger} \longrightarrow \Delta G^{\ddagger} - (G_{TS^{\ddagger}} - G_{E \cdot TS^{\ddagger}}).$$

The combination of substrate and enzyme creates a new reaction pathway whose transition state energy is lower than that of the reaction in the absence of the enzyme (dashed line in Fig. 5.1). Thus enzymes are essentially flexible molecular templates, designed to be complementary to the reactants in their activated transition state geometry, as distinct from their ground–state geometry. Enzymes strongly bind to the transition state, greatly increasing its concentration and accelerating the reaction proportionately.

Much of the catalytic power of enzymes is based on the favorable orientations of the substrates in the enzyme–substrate (E·S) complex. The substrates are bound to a specific region of the enzyme called the *active site*. This region contains the residues that directly participate in the making and breaking of bonds. Although enzymes differ widely in structure, specificity, and mode of catalysis, a number of generalizations concerning their active sites can be stated:

Some key features of active sites

1. The active site takes up a relatively small part of the total volume of an enzyme. Most of the amino acid residues in an enzyme are not in contact with the substrate. This raises the intriguing question of why the enzymes are very large molecules. Nearly all the enzymes are made up of more than 100 amino acid residues, with a diameter of more than 25 Å.

2. Substrates are bounded to enzymes by multiple weak interactions. The non–covalent interactions stabilizing the E·S complex are much weaker than co-

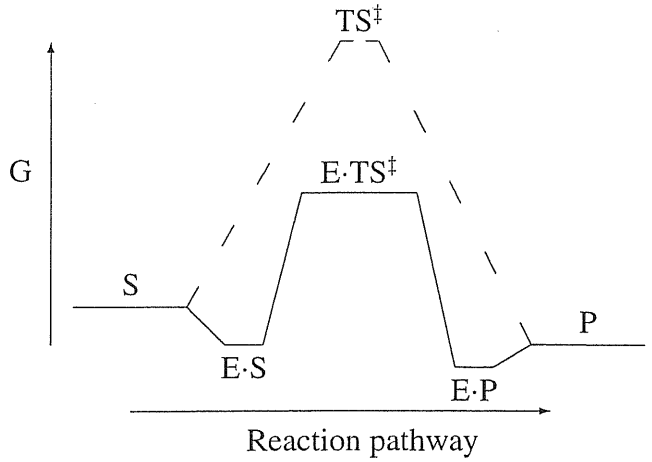

Figure 5.1: Simplified free energy profile of an uncatalyzed reaction (dashed line) and the same reaction catalyzed by an enzyme (solid line). The relative free energies of the substrate S, the transition state TS‡, and the product P are shown when free and when bound to the enzyme E. The reaction is catalyzed by the enzyme when the energy of the transition state is lowered more upon binding to the enzyme than is the energy of the substrate. The relative free energies of S, TS‡, and P when free and when bound depend on their respective affinities for the enzyme and on the concentration of the enzyme. The height of the free energy barrier to the catalyzed reaction is given by the free energy of E·TS‡ relative to E·S; this difference determines the efficiency of the enzyme. The free energy of E·S relative to S is determined by the concentrations of E and S and their affinity; the same considerations apply to E·P and P.

valent bonds, and become significant in binding only when numerous substrate atoms can simultaneously come close to many enzyme atoms. Hence, the enzyme and substrate should have complementary shapes. The directional character of H-bonds between enzyme and substrate often enforces a high degree of specificity.

3. Active sites are clefts or crevices. In all enzymes of known structure, substrate molecules are bound to a cleft or crevice.

5.2 Low–barrier H-bonds and enzymatic catalysis

Enzyme catalysis is commonly attributed to tighter binding between the enzyme and its reactants in the transition state than in initial enzyme–substrate complex. This statement does not, however, explain how an enzyme can bind an intermediate or a transition state much more tightly than the substrate.

After several NMR experiments performed on different enzymatic systems, it has become evident [60–66] that a possible source of the energy can be the formation of very strong H-bonds to the intermediate, while the corresponding H-bonds to the substrate are weak. Two factors are responsible for the strengthening of the H-bond. (*i*) The donor–acceptor distance is reduced, and any competing water is squeezed out by the tight fit of the transition state (and any intermediate that closely resemble it). (*ii*) The proton affinities of the two heteroatoms bridged by the H-bond are brought to near equality.

Strong H-bonds, which Cleland has called "low–barrier hydrogen bonds", can have energies of formation in the gas phase as high as 20 kcal/mol, whereas ordinary H-bonds in biological systems are relatively weak ($\approx$ 3 kcal/mol) [59]. In a weak H-bond the hydrogen is covalently bound to the donor atom, whereas the interaction with the acceptor is largely electrostatic. When the pK_a's of the two atoms are similar, the hydrogen can be attached to either one and there is an energy barrier for the proton transfer. As the distance between the two atoms becomes closer to each other, the barrier between the two hydrogen positions becomes lower and eventually is low enough that the hydrogen can freely move in the space between the two atoms, and its bonding to both atoms becomes essen-

tially covalent [69, 70, 86, 87].

From the above considerations, low–barrier H-bonds have been postulated to stabilize the transition state relative to the ground state. Thus, the H-bond goes from being a low–energy one in the enzyme–substrate complex, to being a high–energy (low–barrier) one in the enzyme–transition state complex, and the energy of the low–barrier H-bond (from 10 to 20 kcal/mol) becomes available to help facilitate the reaction. Because the environment of an enzyme active site is more hydrophobic than that in water, low–barrier H-bonds are expected to provide stabilization energies as in the gas phase, which are known to be very large.

This proposed mechanism based on the formation at the active site of low–barrier H-bonds has been strongly questioned in literature [88–90]. Indeed many quantum–chemical calculations, pioneered by Warshel and Kollmann [91–94], seem to suggest that purely electrostatic, rather than covalent, effects are responsible for the catalytic efficiency of the normal H-bonds present at the active site. In fact enzymes are depicted as "supersolvents" for the charges during the reactions, lowering the free energy of the transition state by an electrostatic stabilization due to a preorganized polar environment in the active site.

In all these calculations—carried out using empirical valence bond or other hybrid quantum mechanics/molecular mechanics methods—the H-bond is described as an electrostatic interaction, handling by the methods of classical electrostatics all the other effects due to the charge distorsion and polarization. The remaining effects, such as the charge transfer between proton donor and acceptor, are strictly quantum mechanical, and are impossible to be simulated within this approach. In this respect, the use of a fully *ab initio* approach—as the one presented in the following chapter—is expected to help shed light on the physical nature of the low–barrier H-bonds.

5.3 Serine proteases: a family of proteolytic enzymes

Proteolytic enzymes are proteins whose function is to decompose other proteins by splitting them into fragments. Within the group of proteolytic enzymes, the serine proteases form an important family whose members are essential to a variety of biological activities: for example, blood coagulation and fibrinolysis, the

release of protein hormones from precursor molecules, the transport of secretory proteins across membranes, the assembly of macromolecular structures such as collagen fibers or certain viruses, fertilization, and the control of proteolytic digestion itself.

Serine proteases are arguably one of the most studied class of enzymes and several excellent review articles [66, 73, 74, 95–103] and books [104–107] were published in the last decades on this subject. We limit ourselves in the following only to a brief description of the main features of serine proteases.

Serine proteases catalyze the hydrolysis of peptide bonds

The chemical bond cut by the serine proteases is the one that joins amino acids together to form proteins. This process of protein decomposition mediated by the serine proteases is the reverse of the process followed in protein synthesis:

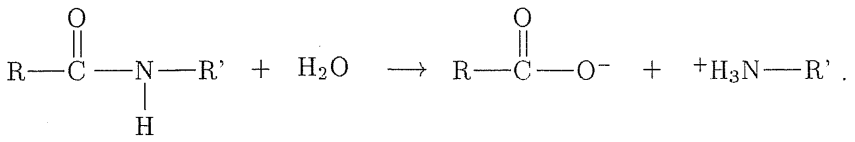

A water molecule (a hydrogen atom and a hydroxyl group) is added for each peptide bond broken, restoring the amino and carboxyl groups at the site of the cleavage to their free amino acid form. Each of the fragments produced by the cutting of the protein is thus a complete peptide, with an amino and a carboxyl terminus. Under physiological conditions the hydrolysis of peptide bonds will proceed in the absence of enzymes, but only at an exceedingly low rate because there is an high energy barrier between the starting materials and the products (if this were not the case, proteins would spontaneously disintegrate).

The ability to make or acquire amino acids and to link them together in the correct sequence to form proteins is one of the fundamental talents of the living cell. Some single–celled organisms, such as bacteria, can synthesize all the required amino acids from simple nutrients. Higher animals, however, have lost the ability to make some of these amino acids and must obtain them from their food supply. Proteolytic enzymes are essential to this process: without them, it would take 50 years to digest a meal.

The digestive enzymes are so extensively investigated mostly because they are easily isolated an purified. Three of them—elastase, trypsin, and chymotrypsin—are serine proteases. They are originate in the pancreas as *zymogens*, or inactive

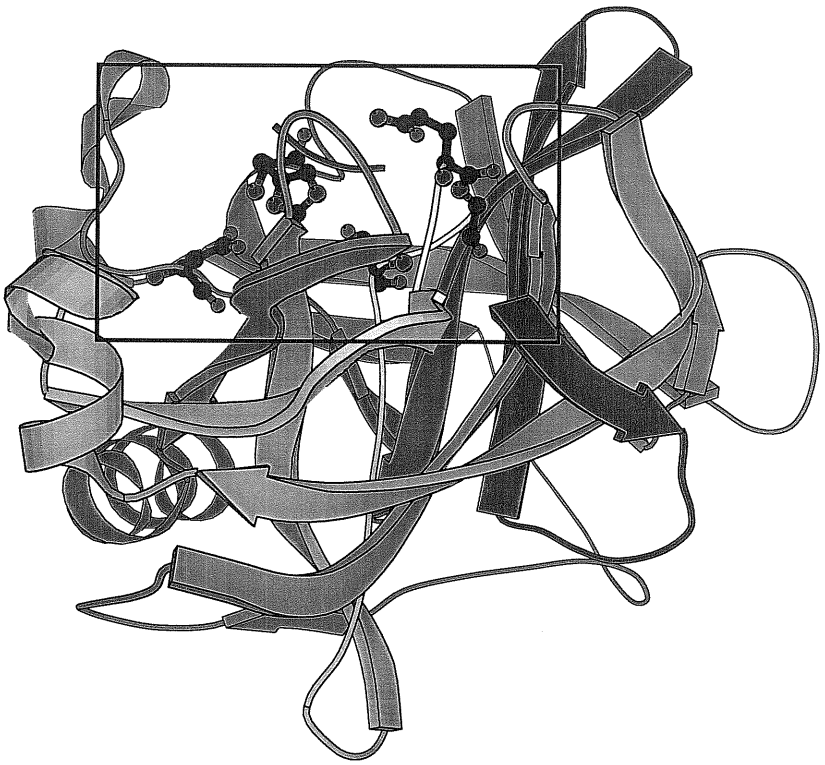

Figure 5.2: Structure of porcine pancreatic elastase complexed with Ace-Ala-Pro-Val-difluoro-N-phenylethylacetamide. The active site region enclosed in the box shows, with a ball–and–stick model, the catalytic triad, the Gln-192 and Gly-193 residues, and the backbone of the inhibitor (purple line).

precursors, which are secreted into the duodenum. There they are activated by the cleavage (catalyzed, in turn, by other proteolytic enzymes) of a specific peptide bond. In concert with other enzymes, the serine proteases ultimately reduce the peptides to individual amino acids, which are absorbed by the intestine and transported to the sites of protein synthesis.

Elastase, trypsin, and chymotrypsin

The digestive enzymes act cooperatively, attacking proteins at different positions. Elastase, trypsin, and chymotrypsin generally act on bonds in the middle of the polypeptide chain. These enzymes are similar in several respects: (1) About 40% of the amino acid sequences of the three enzymes are identical. The degree of identity is even higher (≈60%) for residues located in the interior of the enzymes. (2) X-ray experiments have shown that their three–dimensional structures are very similar. (3) All three enzymes have an identical catalytic mechanism.

Although similar in structure and mechanism, these enzymes differ markedly on substrate specificity. Of the three, trypsin is the most selective: it cleaves only those peptide bonds adjacent to the amino acid units lysine or arginine, which are relatively large, carry a positive charge and are hydrophilic. Chymotripsin is somewhat less specific: it hydrolyzes the bonds adjacent to any of several amino acids that are large but hydrophobic. Elastase acts on bonds adjacent to glycine, alanine or serine, which are the smallest of the amino acids found in nature. Although the three enzymes cannot cut all peptide bonds, they form a team that can reduce any food protein to small, soluble fragments.

X-ray studies have shown that these different specificities are due to quite small structural differences in the binding site. In chymotripsin, a nonpolar pocket serves as a niche for the aromatic or bulky nonpolar side chain. In trypsin, one residue in this pocket is different from chymotrypsin: a serine is replaced by an aspartate. This aspartate in the nonpolar pocket of trypsin can form a strong electrostatic bond with a positively charged lysine or arginine side chain of a substrate. In elastase, the pocket does not exist, as the two glycine residues lining it in chymotrypsin are replaced by the much bulkier valine and threonine.

5.3.1 The catalytic mechanism

The catalytic activity of serine proteases depends on the unusual reactivity of serine 195. This residue, ordinarily rather unreactive under physiological conditions, becomes activated by interactions with histidine 57: these two residues are fundamental for the enzymatic activity and all the serine proteases are inactivated if either of these units is chemically altered in any way. The carboxylate group of aspartate 102, buried in the protein, also is next to histidine 57. These three residues—Ser-195, His-57, and Asp-102—form the *catalytic triad* (see Fig. 5.2 for porcine pancreatic elastase).

Acylation

The commonly accepted mechanism for the catalytic reaction is based on a two–step process: in the *acylation* stage of Fig. 5.3(a)–(c), the oxygen atom of the hydroxyl group of Ser-195 attacks the carbonyl carbon atom of the susceptible peptide bond (R'–NH–CO–R in Fig. 5.3). The carbon–oxygen bond of this carbonyl group becomes a single bond, and the oxygen atom acquires a net negative

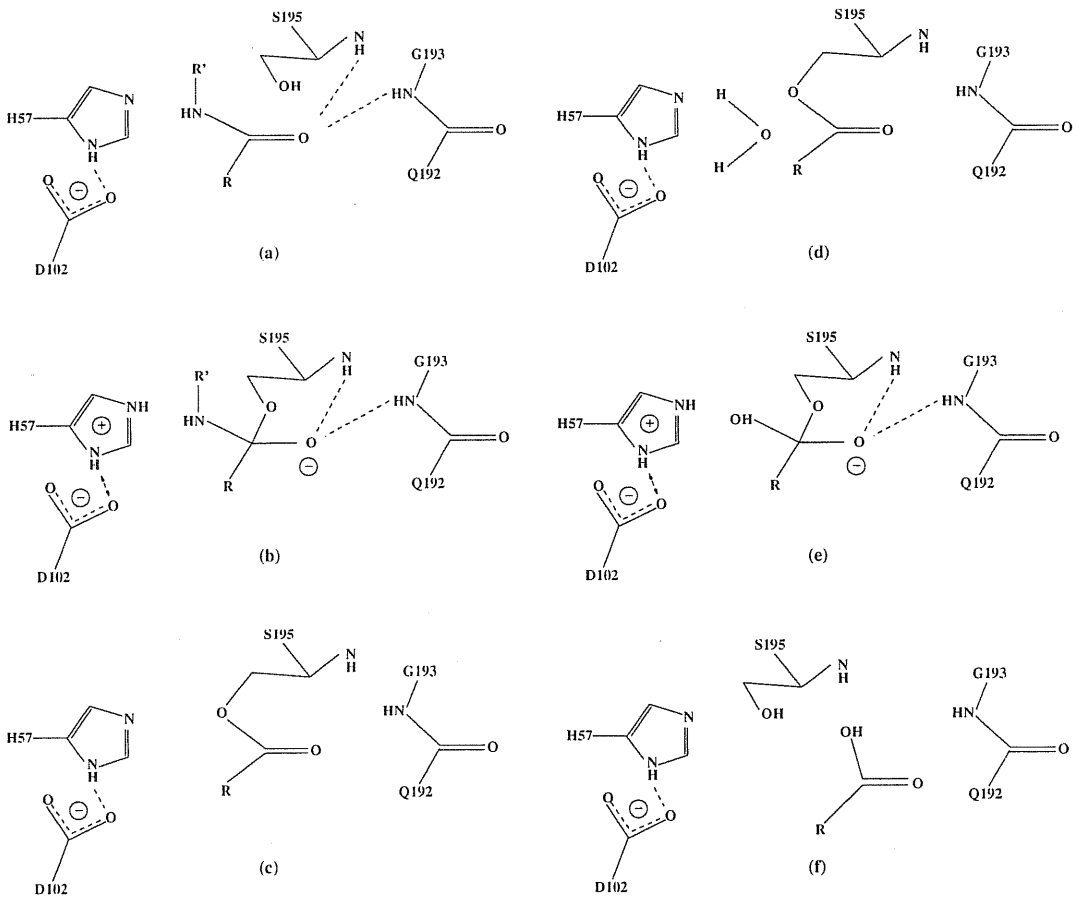

Figure 5.3: Mechanism of hydrolysis catalyzed by serine proteases. Dashed lines indicate H-bonds; in (b) and (e) the double arrow symbol refers to a low–barrier H-bond. (a)–(c) Acylation process: a tetrahedral transition state is formed in which the peptide bond is cleaved. The amine component then rapidly diffuses away, leaving in (c) an acyl–enzyme intermediate. (d)–(f) Deacylation process: the acyl–enzyme intermediate is hydrolyzed by water. The deacylation is essentially the reverse of acylation, with water in the role of the amine component of the original substrate.

charge. The four atoms now bonded to the carbonyl carbon are arranged in a tetrahedron geometry. The formation of this transient *tetrahedral intermediate* from a planar amide group is assisted by the H-bonds between the negatively charged carbonyl oxygen atom (the oxyanion) and the two main chain amide groups of Ser-195 and Gly-193. The essential event favouring the formation of the tetrahedral intermediate is the transfer of a proton from Ser-195 to His-57. This proton transfer is facilitated by the presence of the catalytic triad: Asp-102, forming a strong H-bond with His-57, precisely orients the imidazole ring of His-57 and

partly neutralizes the charge that develops on it during the transition state. The proton held by the protonated His-57 is then donated to the nitrogen atom of the susceptible peptide bond, which thus is cleaved. The amine component (not shown in Fig. 5.3(c)) diffuses away, whereas the acid component of the substrate is esterified to Ser-195.

Deacylation

The next stage, *deacylation* in Fig. 5.3(d)–(f), begins when a water molecule takes the place occupied earlier by the amine component of the substrate. Deacylation is the reverse if acylation, with H_2O substituting for the amine component. First, the charge relay network draws a proton away from water. The resulting OH^- ion immediately attacks the carbonyl carbon atom of the acyl group that is attached to serine 195. As in acylation, a transient tetrahedral intermediate is formed. His-57 then donates a proton to the oxygen atom of Ser-195, which then releases the acid component of the substrate. This acid component diffuses away and the enzyme is ready for another round of catalysis.

Chapter 6

Serine Proteases: an *Ab initio* Molecular Dynamics Study

In serine proteases the H-bond between His-57 and Asp-102, and that between Gly-193 and the transition state intermediate play a crucial role for enzymatic function. To shed light on the nature of these interactions, we have carried out ab initio molecular dynamics simulations on complexes representing adducts between the reaction intermediate and elastase (one protein belonging to the SP family). Our calculations indicate the presence of a low–barrier H-bond between His-57 and Asp-102, in complete agreement with recent NMR experiments on enzyme–transition state analog complexes. Furthermore, comparison with an ab initio molecular dynamics simulation on a model of the substrate–enzyme adduct indicates that the Gly-193–induced strong stabilization of the intermediate is accomplished by charge/dipole interactions and not by H-bonding as previously suggested.

The outline of this chapter is as follows: we briefly analyze the H-bond network present at the active site of serine proteases. Then we describe our structural models of the enzyme–substrate and enzyme–transition state adducts. Finally, we present and discuss our molecular dynamics results.

6.1 H-bond network in serine proteases

Serine proteases (SP) use the catalytic triad (Ser-195–His-57–Asp-102) to catalyze the hydrolysis of peptides (Fig. 5.3). This occurs through nucleophilic addition of the 3-hydroxyl group of Ser-195 to the acyl carbonyl of the substrate, with formation of a negatively charged tetrahedral intermediate (Fig. 5.3b).

Stabilization of the intermediate is achieved by formation of two H-bond with the amide groups of Ser-195 and Gly-193 (for the mammalian isoenzymes [95]) or with the amide groups of Ser-195 and the sidechain of Asn-155 (in the case of bacterial isoenzymes [108]).

Theoretical [92, 109] and experimental [108, 110] studies on wild type and mutants of a bacterial SP (subtilisin) have shown that Asn-155 is a key residue for the biological function, in that it provides a stabilization of the transition state (TS) relative to the ground–state (GS) by as much as $\approx$ 5 kcal/mol. Curiously, no correspondent studies on the mammalian isoenzymes have appeared to shed light on the crucial role of Gly-193[1].

A second, important H-bond interaction involve two residues of the catalytic triad, His-57 and Asp-102. A series of NMR studies on a mammalian [66, 72–74] and bacterial [112] SP's and their complexes with inhibitors have indicated the presence of a low–barrier hydrogen bond (LBHB) linking $N_{\delta 1}$ of protonated His-57 with the β carboxyl group of Asp-102 (double arrow in Fig. 5.3b) [66, 72–74]. Approaching of the TS is suggested to facilitate the formation of the LBHB, which in turn may render $N_{\epsilon 2}$ of His-57 a stronger base for accepting a proton from Ser-195 in the formation of the intermediate [66, 72–74]. As result of this process, the free energy barrier of TS relative to GS decreases. *Ab initio* calculations and neutron scattering experiments have led to the conclusion that the LBHB is very covalent in nature [87]. Thus, this "resonance–stabilization" energy could supply much of the energy necessary for enzyme's catalysis [66, 72–74]. However, the role of this LBHB for the catalytic power of SP's is object of controversy [89, 90].

From the above considerations it is clear that, in spite of its crucial role, the nature and the dynamics of hydrogen bonding in active site of SP are not fully understood. In order to provide a picture of the chemical bonding of these interactions in SP's, and to relate it to the biological function, we have carried out *ab initio* molecular dynamics simulations [69] on models of SP–intermediate and

[1]The H-bond with Ser-195 is much weaker than that of Gly-193. Indeed, analysis of selected SP–transition state analog complexes (entries 1AI8,1VCG,4EST,1GMH,1SGC,1PO3,7GCH of the Protein Data Bank [111]) shows that 2.8 $\leq$d(N(Ser-195)$\cdots$O) $\leq$ 3.2 Å and 121^o $\leq$ $\angle$(N(Ser-195)H$\cdots$O) $\leq$ 157^o and 2.6 $\leq$ d(N(Gly-193)$\cdots$O) $\leq$ 2.9 Å and 150^o $\leq$ $\angle$(N(Gly-193)H$\cdots$O) $\leq$ 160^o (H atoms obtained assuming standard bond lengths and bond angles).

SP–substrate complexes. Anticipating our results, the calculations show that the LBHB is a strongly covalent interaction and that the dramatic Gly-193–induced stabilization of the reaction intermediate is due mainly to the electrostatic interactions between the intermediate and the Asn-192–Gly-193 peptide's unit dipole.

6.2 Computational procedure

6.2.1 Model complexes

Our structural models for the adducts of SP with intermediate (I·SP) and substrate (S·SP) are based on the X-ray structure of porcine pancreatic elastase complexed with Ace-Ala-Pro-Val-difluoro-N-phenylethylacetamide (PDB entry: 4EST) [111, 113]. They include the entire catalytic triad, the scissile peptide bond and the oxyanion hole.

The construction of the complexes is carried out in several steps: *i)* the terminal N-phenylethylacetamide is replaced by an acetyl group; *ii)* all hydrogen atoms of the complex, not present in the X-ray structure, are added assuming standard bond lengths and bond angles; *iii)* a shell of 1453 water molecules, including the crystallographic ones, is added; *iv)* four chlorine counter ions are added to ensure neutrality; *v)* energy minimization is carried out with the AMBER suite of programs [114] using the AMBER force field [115] (convergence criterion 0.0001 kcal/(mol·Å)). In the minimization, no periodic boundary condition are applied and the electrostatic interactions are calculated assuming a constant dielectric function $\epsilon = 1$ and without cutoff. The resulting structure is reported in Fig. 5.2.

The I·SP and S·SP model complexes comprises the entire side-chain of Asp-102, the imidazole ring of His-57, the Q192G193 peptide linkage and the entire Ser-195 residue, which in I·SP is covalently bound to the substrate (Fig. 6.1a,b). His-57 is considered doubly protonated in I·SP and protonated in the δ position in S·SP [116].

Alternative models representing I·SP and S·SP differ from the previous ones for the substitution of the Q192G193 peptide link with dimethylammonia (Fig. 6.1 c,d).

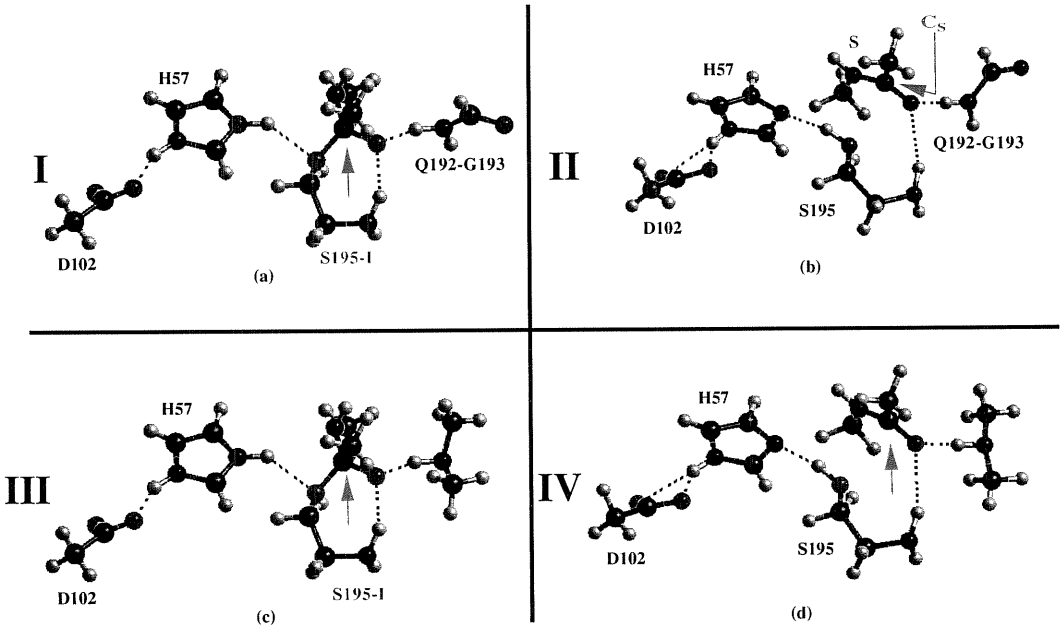

Figure 6.1: Model complexes representing I·SP ((a) and (c)), S·SP ((b) and (d)). In (c) and (d) the Q192G193 peptide unit is replaced by dimethylammonia. H-bonds are depicted with dashed lines. Green arrows indicate the scissile carbon atom C_S. The latter is labeled only in (b) for clarity. Color conventions as follows: black balls represent carbon atoms, red balls oxygen, blue balls nitrogen, and grey balls hydrogen.

6.2.2 Calculations

The quantum–mechanical problem is solved within the framework of DFT–KS formulation. The KS orbitals are expanded in a plane–wave basis set, up to an energy cut–off of 70 Ry. Only valence electrons are considered explicitly, pseudopotentials of the Martins and Troullier [117] being used for the core–valence electron interaction. BLYP [118, 119] gradient–corrected exchange–correlation functionals are used. The charge of all the complexes is -1.

We have carried out geometry optimization using the direct inversion in iterative subspace (DIIS) method [120, 121] for both electronic (convergence threshold set to 10^{-5}) and ionic degrees of freedom (convergence threshold set to $5 \cdot 10^{-4}$).

DFT–based Car–Parrinello *ab initio* molecular dynamics simulations are performed at constant temperature, with the atomic trajectories collected over a period of 0.6 and 1.0 ps for S·SP and I·SP, respectively. Equations of motion are integrated with the velocity Verlet algorithm. The fictitious electron mass is 400

a.u. and the integration timestep is 4 a.u. Constant temperature simulations are achieved by coupling the systems to a Nosé thermostat [122] at $T = 300K$ with a frequency of 500 cm^{-1}. The terminal hydrogens of Asp-102, His-57, and Gly-193, corresponding to the C_α, C_β and C_α respectively, are kept fixed in their starting position; in S·SP an additional constraint between the O_γ(Ser-195) and the substrate carbon of the scissile bond (indicated in Fig. 6.1b as C_S) is imposed.

Calculations including the external electrostatic potential of the whole protein–water system are also carried out. This potential $\Phi_{prot}(\mathbf{r})$ at the point $\mathbf{r}$ is evaluated as

$$\Phi_{prot}(\mathbf{r}) = \sum_i \frac{q_i}{|\mathbf{r}_i - \mathbf{r}|} \tag{6.1}$$

where q_i are the RESP [123] atomic point charges at point $\mathbf{r}_i$.

The electrostatic energy ΔE between to moieties (e.g. the intermediate and the Q192G193 peptide unit) is calculated as

$$\Delta E = \sum_{ij} \frac{q_i q_j}{r_{ij}}, \tag{6.2}$$

where the indexes i and j refer to atoms of the two moieties. q_i and q_j are the partial atomic ESP charges [124] and r_{ij} is the interatomic distance. Test calculations are carried out also using the multipolar expansion of the electrostatic energy up to the dipolar term:

$$\Delta E \simeq Q_1 \Phi_2 - \boldsymbol{\mu_1} \cdot \mathbf{E_2}. \tag{6.3}$$

where Q_1 and $\boldsymbol{\mu_1}$ are charge and dipole moments of moiety 1 and Φ_2 and $\mathbf{E_2}$ the electric potential and the electric field produced by moiety 2, respectively. The results turn out to be very similar to those obtained with Eq. 6.2.

Binding energies (B.E.'s) are calculated as total energies differences between complexes in Fig. 6.1 and their forming elements. The B.E. of complexes **I** and **III** could not be determined because of the instability of the intermediate fragment.

All Car–Parrinello calculations presented in this chapter are performed with a parallel version of the CPMD code, version 3.0h [125].

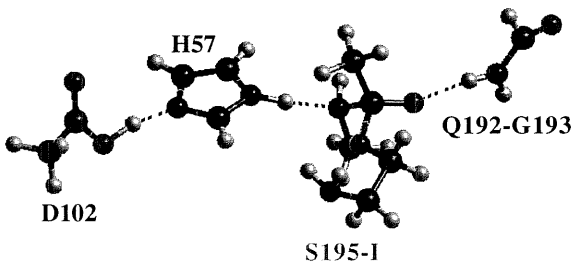

Figure 6.2: Molecular dynamics of I·SP: final structure of model **I**. H-bonds are represented with dashed lines. Color conventions as in Fig. 6.1.

6.3 Results

In this section, first we analyze structural and electronic features of two models representing the adduct between serine protease and the reaction intermediate (**I** and **III** of Fig. 6.1). Comparison is then made with features of models of the substrate–enzyme complex (**II** and **IV** of Fig. 6.1).

6.3.1 The intermediate–enzyme complex

Structural features and charge distribution

Conformational properties as well as the H-bond network of the complex are fairly maintained during the dynamics (Fig. 6.2). Consequently, the charge distribution does not change significantly (with exception of C_S and N_S, corresponding to the site of bond cleavage), as indicated by the ESP atomic partial charges reported for several snapshots of the molecular dynamics (Tab. 6.1). Note that the C_S–O bond of the intermediate is very polarized towards the oxygen, consistently with the fact that this bond is to be broken in the subsequent step of the hydrolysis. The presence of the protein field does not affect significantly the charge distribution (Tab. 6.2), suggesting that solvent effects do not play a major role for the electrostatic interaction at the active site.

H-bond pattern: Asp-102–His-57

During the dynamics, proton hopping occurs between the His-57 and Asp-102 in the subps time–scale (Fig. 6.3). The presence of a LBHB is completely consistent with NMR data on an intermediate–serine protease complex, namely the peptidyl trifluoromethyl ketone–chymotrypsin adduct [72].

As already stressed in the previous chapter, the "signature" for the presence of a low–barrier H-bond between the two residues is the covalent nature of the

Time (ps)	O_γ(S195)	C (S)	N (S)	O (S)	N (G193)	C (Q192)	O (Q192)
Init.	-0.511	1.194	-0.802	-0.717	-0.603	0.504	-0.631
0.1	-0.509	1.202	-0.529	-0.837	-0.733	0.597	-0.649
0.2	-0.461	1.022	-0.237	-0.724	-0.646	0.571	-0.630
0.3	-0.328	0.835	0.006	-0.658	-0.556	0.516	-0.631
0.4	-0.342	1.083	-0.193	-0.754	-0.582	0.507	-0.625
0.5	-0.372	1.146	-0.201	-0.794	-0.558	0.505	-0.616
0.6	-0.407	1.233	-0.480	-0.829	-0.615	0.578	-0.654
0.7	-0.430	1.174	-0.311	-0.883	-0.570	0.563	-0.638
0.8	-0.551	1.245	-0.401	-0.843	-0.487	0.478	-0.620
0.9	-0.504	1.124	-0.202	-0.772	-0.503	0.502	-0.634
1.0	-0.399	1.074	-0.245	-0.827	-0.593	0.636	-0.694
Average	-0.438	1.121	-0.327	-0.785	-0.586	0.542	-0.638
St. Dev.	0.072	0.112	0.207	0.064	0.064	0.048	0.021

Table 6.1: Selected ESP partial atomic charges of I·SP *in vacuo*.

Time (ps)	O_γ(S195)	C (S)	N (S)	O (S)	N (G193)	C (Q192)	O (Q192)
0.1	-0.513	1.154	-0.531	-0.876	-0.646	0.640	-0.750
0.2	-0.453	0.931	-0.261	-0.677	-0.527	0.595	-0.722
0.3	-0.329	0.649	-0.037	-0.580	-0.410	0.481	-0.692
0.4	-0.381	0.961	-0.036	-0.739	-0.430	0.400	-0.644
0.5	-0.412	1.000	-0.106	-0.773	-0.358	0.341	-0.611
0.6	-0.482	1.270	-0.305	-0.929	-0.460	0.447	-0.657
0.7	-0.439	1.267	-0.295	-0.932	-0.354	0.504	-0.714
0.8	-0.602	1.373	-0.382	-0.843	-0.349	0.462	-0.720
0.9	-0.606	1.292	-0.221	-0.719	-0.290	0.494	-0.729
1.0	-0.493	1.076	-0.308	-0.802	-0.417	0.596	-0.793
Average	-0.471	1.097	-0.248	-0.787	-0.424	0.496	-0.703
St. Dev.	0.084	0.208	0.148	0.107	0.097	0.088	0.051

Table 6.2: Selected ESP atomic charges of I·SP in the presence of the protein electrostatic potential.

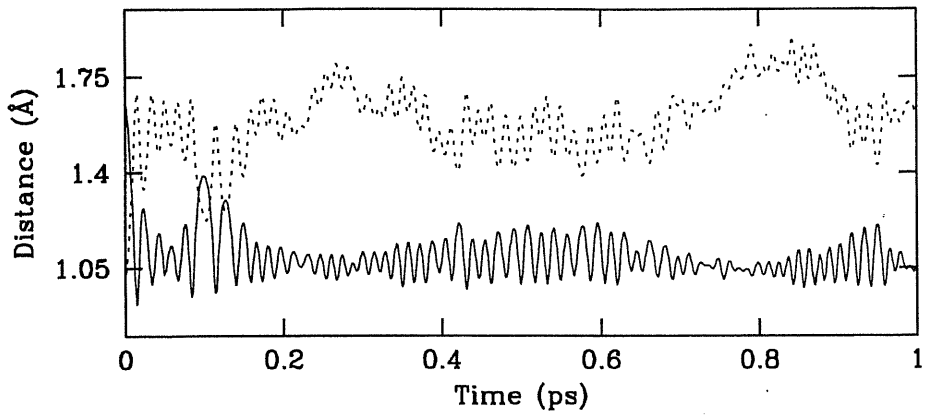

Figure 6.3: His-57–Asp-102 H-bond in I·SP (complex **I**): H–$O_{\delta 2}$(Asp-102) (solid line) and H–$N_{\delta 1}$(His-57) (dashed line) distances plotted as a function of time.

bonding. This corresponds to a quantum mechanical superposition of the two forms, representing the two possible hydrogen positions: the hydrogen is free to jump from one atom to the other, leading to great resonance stabilization.

The ELF is the simplest tool at our disposal for a first principles analysis of the chemical bond and a series of ELF plots along the proton jumping reveals the strong covalent nature of the LBHB between His-57 and Asp-102. Fig. 6.4 shows the ELF before, during and after the proton transfer from one residue to the other. The red areas indicate strong localization, *i.e.* spatial regions where the Pauli principle has little influence on the electron distribution and the electrons locally behave as a system of bosons at the same density.

Fig. 6.4a shows the presence of the lone pairs of the aspartate oxygen and of the strong electron localization along the histidine $N_{\delta 1}$–H bond, which indicates the covalent nature of the bond. During the proton transfer (Fig. 6.4b), the $N_{\delta 1}$–H bond is still very covalent and an incipient *covalent* $O_{\delta 2}$–H bond is being formed. Protonation of Asp-102 establishes a covalent O–H bond: significant portion of ELF is indeed localized on the H atom (Fig. 6.4c). The formation of the nitrogen electron lone–pair is also evident from the picture. We conclude that the bonding in this LBHB is essentially covalent in nature. Similar findings have been reported in a series of very recent *ab initio* studies of low–barrier H-bonds in an organic molecule [70, 87].

H-bond pattern: Gly-193–intermediate

The second fundamental H-bond interaction investigated here involves Gly-

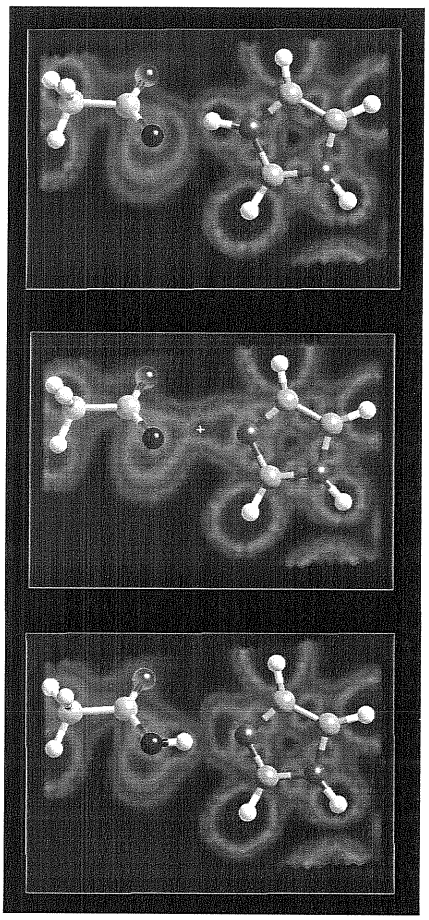

Figure 6.4: His-57–Asp-102 proton transfer: electron localization function (ELF) of three snapshot during the dynamics. The ELF is represented in a best–fit plane containing the oxygen, the proton and the imidazole ring, and it ranges from 0 (blue) to 1 (red).

193 and the intermediate carbonyl oxygen. This H-bond is well maintained during the dynamics (average O· · ·H distance of 1.7(0.1) Å). A rough estimation of the interaction energy based on the electrostatic model of Eq. 6.2, indicate that Gly–193 stabilizes the intermediate by more than 10 kcal/mol (Tab. 6.3). This value appears to be too large for a purely electrostatic H-bond interaction [59, 91].

Inspection of the structure reveals that the very large Q192G193 peptide's unit dipole ($\approx$ 4 D [106]) could be also an important factor for intermediate stabilization, as it points towards the negative charge of the intermediate. To extract the peptide dipolar contribution from the total stabilization energy we construct a second model complex in which the Q192G193 peptide unit is substituted by

	ESP	B.E.
ΔE (I·SP) (Complex **I**)	-12(4)	—
ΔE (I·SP) (Complex **III**)	-2.6	—
ΔE (S·SP) (Complex **II**)	-6(2)	-4.2
ΔE (S·SP) (Complex **IV**)	-2.6	-1.5

Table 6.3: Intermediate – and substrate – Q192G193 peptide unit interactions. Energies (kcal/mol) are calculated from the electrostatic ESP–based model and from binding energies (see Computational Section). ESP–based energies of complexes **I** and **II** are calculated as average during the dynamics, whereas those of complexes **III** and **IV** from the initial structural model.

dimethylammonia (**III** in Fig. 6.1c). Tab. 6.3 shows that the resulting stabilization is much smaller, only few kcal/mol. Thus, we conclude that a large contribution of the transition state stabilization is due to electrostatic interaction (charge–dipole interactions).

To study the relevance of the Q192G193 dipole *on the dynamics*, an ab initio molecular dynamics simulation on complex **III**, where the Q192G193 peptide unit is replaced by a dimethylammonia, is performed. Fig. 6.5, which reports structural properties of the complex, indicate that this complex is very unstable with respect to the substrate–enzyme complex. Indeed, while the key Gly-193–intermediate H-bond becomes very weak(Fig. 6.5a), the protonated His-57 transfers a proton to the intermediate (Fig. 6.5a) and the O_γ(Ser-195)–C_S bond of the intermediate breaks. As a result, a double C_S–O(I) bond is formed (as indicated by the decrease of the bond distance up to the typical value of a carbonyl peptide bond (1.25 Å in Fig. 6.5b)) and C_S changes it hybridization from sp^3 to sp^2, with formation of the planar peptide unit (as shown by the increase of the ∠(N(I)–C_S–O(I)) angle up to $\approx 120^o$ (Fig. 6.5c)). In conclusion, our calculations suggest that the absence of the stabilizing Q192G193 dipole causes the reverse of the reaction, with formation of the substrate and the original H-bond pattern of the catalytic triad.

6.3.2 The substrate–enzyme complex

Gln-192–substrate interactions

To estimate the stabilization of the Q192G193 peptide unit's dipole on the substrate, we have performed an *ab initio* molecular dynamics simulation of a model

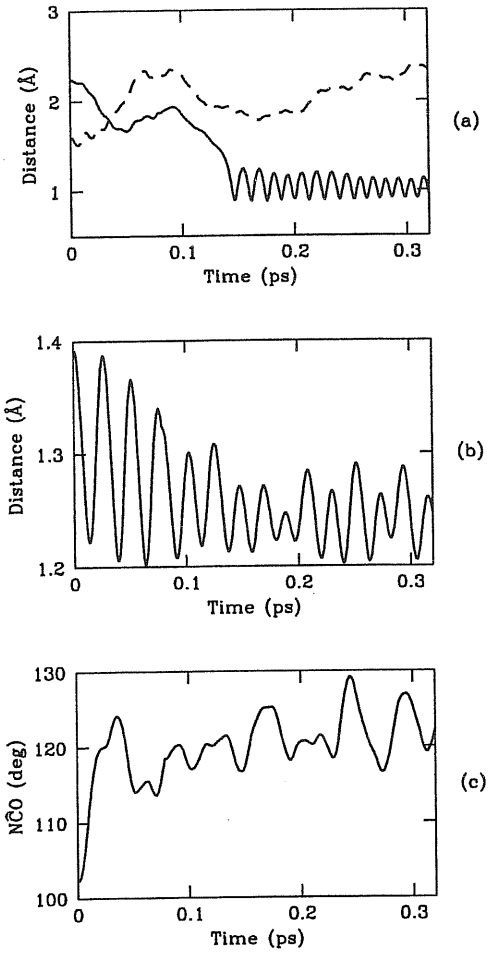

Figure 6.5: Molecular dynamics of I·SP: selected structural properties of complex **III** plotted as a function of time. (a) H(Gly-193)–O(I) (dotted line), $H_{\epsilon 2}$(His-57)–O_{γ}(Ser-195) (solid line) distances; (b) C_S–O(I) bond length; (c) N(I)–C_S–O(I) angle.

of the enzyme–substrate adduct (**II** in Fig. 6.1b).

Fig. 6.6 shows that during the dynamics the two key H-bond interactions are maintained but no proton transfer occurs. Interestingly, the substrate–protein interaction energy turns out to be much lower than that of the I·SP complex (Tab. 6.3). Replacing the Q192G19 peptide with dimethylammonia (complex **IV**) causes a drastic decrease of the interaction energy. The latter turns out to be practically identical to that of complex **III** (Tab. 6.3). We conclude that the H-bond

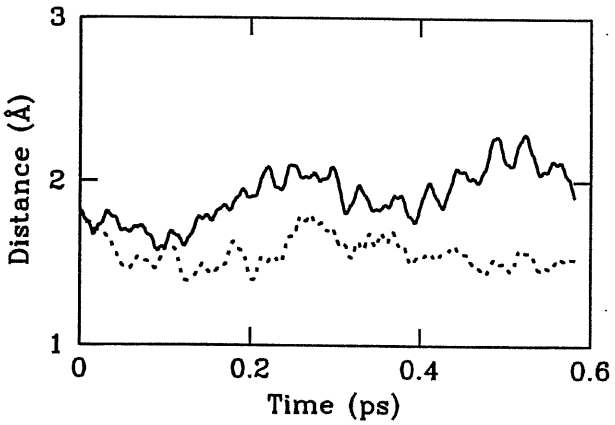

Figure 6.6: H-bonding of S·SP (complex **II**): H(Gly-193)–O(S) (solid line), $O_{\delta 2}$(Asp-102)–$H_{\delta 1}$(His-57) (dotted line) distances plotted as a function of time.

interaction are similar in the S·SP and I·SP complexes. In contrast, the electrostatic (charge–dipole) interactions are very different, the I·SP being more stable by $\approx$ 6 kcal/mol than S·SP (Tab. 6.3). It is interesting to note that this value compares well with previous quantum mechanical calculations for the Asn-155–TS stabilization in the bacterial isoenzyme [92, 109]. We conclude that *the transition state stabilization is due mostly to charge–dipole interactions.*

For these complexes it has been possible to calculate also the binding energies. Tab. 6.3 shows a qualitative agreement between binding energies and energies based on electrostatic model. This validates the use of the electrostatic model for a qualitative analysis of intermolecular interactions, as it has been done in this work.

Charge Distribution

Also in this complex, most of the ESP charges do not vary significantly during the dynamics and by introducing the electric field of the protein (Tabs. 6.4 and 6.5). Most of the ESP charges turn out to be similar to those of the I·SP complex. A notable exception is represented by the C–O peptide bond, which in this case is much less polarized toward the oxygen. Thus it appears that the protein active site, and in particular the Q192G193 moiety, is engineered so as to render the scissile bond more polar in the formation of the transition state.

Time (ps)	O_γ(S195)	C (S)	N (S)	O (S)	N (G193)	C (Q192)	O (Q192)
Init.	-0.468	0.635	-0.352	-0.469	-0.561	0.585	-0.637
0.1	-0.473	0.739	-0.527	-0.559	-0.709	0.624	-0.644
0.2	-0.410	0.578	-0.259	-0.574	-0.595	0.599	-0.635
0.3	-0.528	0.684	-0.280	-0.595	-0.638	0.605	-0.640
0.4	-0.476	0.585	-0.219	-0.519	-0.642	0.633	-0.643
0.5	-0.491	0.618	-0.165	-0.577	-0.592	0.630	-0.658
0.6	-0.355	0.576	-0.189	-0.549	-0.628	0.616	-0.644
Average	-0.457	0.631	-0.284	-0.549	-0.624	0.613	-0.643
St. Dev.	0.053	0.057	0.114	0.040	0.044	0.016	0.007

Table 6.4: Selected ESP atomic charges of S·SP *in vacuo*.

Time (ps)	O_γ(S195)	C (S)	N (S)	O (S)	N (G193)	C (Q192)	O (Q192)
Init.	-0.331	0.693	-0.474	-0.488	-0.614	0.686	-0.645
0.1	-0.418	0.703	-0.602	-0.552	-0.701	0.745	-0.782
0.2	-0.349	0.492	-0.389	-0.513	-0.574	0.722	-0.768
0.3	-0.477	0.601	-0.356	-0.546	-0.667	0.825	-0.789
0.4	-0.475	0.561	-0.301	-0.495	-0.650	0.812	-0.765
0.5	-0.455	0.553	-0.262	-0.524	-0.570	0.772	-0.787
0.6	-0.341	0.496	-0.273	-0.497	-0.650	0.775	-0.769
Average	-0.407	0.586	-0.380	-0.516	-0.632	0.762	-0.758
St. Dev.	0.060	0.079	0.114	0.023	0.045	0.045	0.047

Table 6.5:

Selected ESP atomic charges of S·SP in the presence of the protein electrostatic potential.

6.4 Discussion

Within the very short time–scale here explored, our *ab initio* molecular dynamics simulations help elucidate important aspects of two key interactions in serine proteases–reaction intermediate complexes, the His-57–Asp-102 LBHB and the Gly-193–intermediate H-bonds.

Our calculations are completely consistent with and confirm the existence of a LBHB between His-57 and Asp-102, which has been observed experimentally in transition state analog inhibitor complexes [66, 72–74]. Furthermore, they strongly support the proposal of an LBHB–facilitated mechanism [72]. Indeed, the LBHB turns out to be mostly covalent in nature. The energy supplied by covalent interaction may be crucial to overcome the energy loss due to the compression of the two residues, which is a prerequisite of the postulated LBHB–based reaction [72].

The second conclusion of our molecular dynamics approach is that, the rather large Gly-193–induced stabilization of the transition state with respect to the fundamental state *is not* caused by an H-bond with Gly-193, as commonly proposed [95, 96]: indeed, the H-bond favors the binding of *both* substrate and intermediate by $\approx$ 2.6 kcal/mol, a value typical of a strong H-bonds in biological systems [59]. Instead, the negatively charged transition state turns out to be more stable relative to S·SP by several kcal/mol as a result of the interaction of the negative charge with the large dipole of the Q192G193 peptide unit. A simulation in which dimethylammonia replaces the Q192G193 peptide unit confirms the crucial role of the dipole: the absence of the stabilizing charge–dipole interaction renders the intermediate species unstable. These considerations suggest that site–directed mutagenesis experiments on the 192 and/or 193 positions might affect significantly the activity of SP, as the Q192G193 dipole orientation may be not optimal for transition state stabilization.

Because environment effects may be very important for the chemistry of the active site of this and other enzymes [91–93, 109], we carry out some of the calculations in the presence of the electric field of the protein. Our results, summarized by tables 6.1–6.2 and 6.4–6.5, indicate however that the field appears not to affect dramatically the charge distribution of the I·SP and S·SP complexes. More

sophisticated models of the protein electric field, which for instance include the electronic polarizabilities of the protein atoms, are not expected to alter significantly the picture.

Conclusions

Since its first introduction in 1990 by Becke and Edgecombe in the context of a new theoretical definition of localized atomic quantum shells, the electron localization function (ELF) has rapidly become, in the quantum chemical literature, a very popular tool to analyze localization properties and chemical bonding. The applications of ELF presented in this thesis to molecules, bulk systems, solid surfaces, and impurities, clearly show the unique ELF ability to provide—without using any spectral information, being the ELF a pure ground–state property—a meaningful description of the chemical bond for several different classes of materials.

In particular, the choice of the pseudopotential scheme—which is of universal use in modern condensed matter theory to eliminate the heavy computational burden associated to the chemically inert core electrons—makes the ELF message particularly simple and transparent.

Basically the ELF can be considered as a suitable measure of how the kinetic energy density, by the effect of Pauli principle, locally deviates from an appropriately defined "bosonic" lower bound. We have exploited this feature in a novel geometric solution to the N-representability problem for an extended system, which implies an explicit form for the Kohn–Sham kinetic energy functional in terms of the density [11]. The ELF is intimately related to this approximate functional, whose value strongly depends on the nature of the chemical bonding in the material.

Besides this general analytical result, in this thesis we have also presented several original applications of ELF in condensed matter systems, as well as to systems of biological interest.

We have investigated how the ELF portrays the bond rearrangement occurring

at a crystal surfaces. We have analyzed two paradigmatic cases, corresponding to the two very opposite bonding characters perspicuously visualized via an ELF approach: namely, the covalent and the metallic bond. At a semiconductor surface the electronic system changes its character upon reconstruction: the ELF clearly describes how electron pairing accompanies rebonding [12]. At a metal surface the bonding character strongly depends on the local coordination and packing. The ELF, calculated for surfaces of a typical *sp*–bonded metal, distinctly reveals the rearrangement in the electron distribution due to the surface formation and to the changes in the local coordination [13].

We have also proposed the immediate graphical language of ELF as a unique tool for investigating bonding in the presence of defects, either in crystals or in much more complicated systems, such as disordered clusters or amorphous materials. In particular, we have shown that a combined analysis of the electronic charge density distribution and ELF allows to unambiguously classify the different kind of electronic defects present in amorphous silicon samples [14].

Finally, the ELF has turned out a useful tool even for a typical biochemical problem, such as the study of the hydrogen bond pattern present the active site of serine proteases, an important and large family of digestive enzymes. Through an *ab initio* molecular dynamics study [69], we confirm the existence of "low–barrier" (i.e. short, very strong) hydrogen bonds between two conserved residues at the active site and our ELF analysis clearly reveals the strong covalent nature of these bonds.

In conclusion, we propose here the immediate graphical ELF language as a unique tool to understand electron localization and chemical bonding in a wide variety of physical systems, ranging from simple molecules, to surfaces, impurities and large biological complexes. In all these systems, the ELF yields a very meaningful, easily understandable and visually informative analysis of the chemical bonds.

Acknowledgments

At the end of this wonderful experience here in Sissa, it is a great pleasure for me to acknowledge all the people that have contributed to this work, as well as all the other friends that have been always so close to me during these years.

First, I want to thank my supervisors Raffaele Resta and Paolo Carloni, for teaching me a lot of physics (and chemistry!), for guiding my very first steps in the research field, and for being always so patient. Both of them, in different manner, have been an example and have transmitted me a contagious enthusiasm for this work.

I owe special thanks to Maria Peressi, for always being so nice and for her precious suggestions (actually, not only about amorphous systems!).

Now it is time to thanks a lot of people, not directly involved in this work, that have been very important for these years here in Trieste, and which I will never forget (strictly, *not* in order):

Marco Saitta, without whom our life here in Sissa would never be the same: he was the official organizer (in italian, *Filini*) of every social activity, and also an invaluable source of moral support and scientific help. Alice Ruini was always so nice with me: every time that something went wrong, Alice was there, ready to help me. Daniele, with his (sometimes terrible) jokes is always so funny and I will never forget his e-mails, or the (yet) famous "Monsieur–Tebaldì" joke.

I want also to acknowledge the friendship with Cecilia Clementi and her little–kangaroo, the "all–American" Giovanni Fossati, Barbara Montanari for always being so pleasant, and Franz Di Tolla for being so incredibly kind to everyone.

I want to remember all the other friendly people that I knew in Trieste, with whom I shared such a good time: Stefano "Tex" Martinelli and Daniela, Claudio "Tebby" Tebaldi, Carlo "Charles" Cavazzoni, Marco Fornari, Claudia Bun-

garo, Sabrina Gustin, Stefano de Gironcoli and Silvia, Leonardo Guidoni and Silvia, Frank Alber, Stefano Lise, Alessandro Laio, Stefano Giovanazzi, Antonio Trovato, Catia Lavalle, Valentina D'Odorico, Guido Chiarotti, Stefano Baroni, Gabriele Cipriani, Luca Capriotti, Massimo Capone, Stefano Piana, Carlo Acerbi, Federico Becca, Stefania De Palo, Gianluca "Giallo" Israel, Chiara Leone, Maria Stella Gelli, Pierluigi "PiGi" Monaco, Sandro Scandolo, and many, many other...

A very special thanks to Matteo "Matteuccio" Calandra, one of the most friendly person that I have ever met: during these years, he was not only a perfect house–mate, but a precious friend. I will never forget his enthusiasm and optimism, and I am sure that he will have a bright future in Germany (and not only in Germany).

I want to acknowledge the "special" friendship of Roberto and Agata.

Finally, I conclude with my wife Antonella for being always with me.

Appendix A

Density Functional Theory

A.1 Hohenberg–Kohn theorem and Kohn–Sham formulation

From the microscopic point of view, atoms, molecules and solids consist of interacting ions and electrons, and their properties could be in principle determined by solving the Schrödinger equation. In practice, this is not feasible, and the solution of the problem requires several approximations. Firstly, the Born–Oppenheimer (or adiabatic) approximation [126, 127] is introduced, which states that, because of the large difference between electronic and ionic masses, the nuclei can be described as fixed charges in the treatment of the electronic problem, so that their coordinates appear in the Hamiltonian only as parameters. The electrons move in the "external" potential $V_{\text{ext}}(\mathbf{r})$ of the nuclei, following adiabatically their slow motion and remaining close to the quantum–mechanical ground–state. An N-electrons system is therefore described by the Hamiltonian (atomic units ared used throughout):

$$\mathcal{H} = -\frac{1}{2}\sum_{i=1}^{N}\nabla_i^2 + \sum_{i=1}^{N}V_{\text{ext}}(\mathbf{r}_i) + \frac{1}{2}\sum_{i\neq j}\frac{1}{|\mathbf{r}_i - \mathbf{r}_j|}. \tag{A.1}$$

The density functional theory (DFT) provides an appropriate mathematical framework for determining the ground–state of a many–electron system, which is the only required knowledge for the study of a great number of physical prop-

erties. More details about this theory can be found in several review papers and books [16, 20, 128, 129]. For the present purpose we limit ourselves to the basic findings.

The DFT is based on the Hohenberg–Kohn theorem [18], which consists of two statements:

- The external potential V_{ext} acting on a system of electrons is determined (up to an additive constant) by the ground–state electronic charge density $n(\mathbf{r})$ *alone*.

As a consequence, also $E = \langle\Psi|\mathcal{H}|\Psi\rangle$, where Ψ is the N-particle wavefunction, is a unique functional of $n(\mathbf{r})$, and can be written as:

$$E[n] = \int d\mathbf{r}\, V_{\text{ext}}(\mathbf{r}) n(\mathbf{r}) + F[n], \tag{A.2}$$

where $F[n]$ does not depend on the external potential, *i.e.* it is *universal.*

- The ground–state total energy E_{GS} of the system is the minimum of the functional $E[n]$ with respect to variations of the electronic charge density $n(\mathbf{r})$.

In this framework, the determination of the ground–state of the system is reduced to the minimization of $E[n]$ under the constraint

$$\int d\mathbf{r}\, n(\mathbf{r}) = N, \tag{A.3}$$

i.e. to the solution of the Euler–Lagrange equation:

$$\frac{\delta}{\delta n}\left[E - \mu \int d\mathbf{r}\, n(\mathbf{r})\right] = 0, \tag{A.4}$$

where the Lagrange multiplier μ is introduced to impose the condition in Eq. (A.3).

The usual implementation of the DFT is due to Kohn and Sham (KS) [19] who wrote the electron density in terms of an orthonormal set of N independent one–particle wavefunctions ψ_i, the *KS orbitals:*

$$n(\mathbf{r}) = \sum_{i=1}^{N} f_i |\psi_i(\mathbf{r})|^2, \tag{A.5}$$

where f_i are the occupation numbers. In the KS formulation the universal functional $F[n]$ is then written in the form:

$$F[n] = T_s[n] + \frac{1}{2}\int d\mathbf{r}d\mathbf{r}' \frac{n(\mathbf{r})n(\mathbf{r}')}{|\mathbf{r}-\mathbf{r}'|} + E_{xc}[n]. \tag{A.6}$$

Here $T_s[n]$ is the kinetic energy that a system with density $n(\mathbf{r})$ would have in the absence of electron–electron interaction. The second term in the r.h.s. of Eq. (A.6) is the classical (Hartree) electrostatic term. The expression (A.6 defines the so called *exchange–correlation energy* E_{xc}, which is the unknown part of the problem. If we assume the KS orbitals to be our basic variables, the solution for the Euler–Lagrange equation (A.4) can be found by solving a set of coupled single–particle Schrödinger–like equation for noninteracting electrons:

$$\Big(-\frac{1}{2}\nabla^2 + \underbrace{V_{ext}(\mathbf{r}) + V_H(\mathbf{r}) + v_{xc}(\mathbf{r})}_{V_{KS}(\mathbf{r})} \Big)\psi_i(\mathbf{r}) = \epsilon_i\psi_i(\mathbf{r}), \tag{A.7}$$

where:

$$V_H(\mathbf{r}) = \int d\mathbf{r}' \frac{n(\mathbf{r}')}{|\mathbf{r}-\mathbf{r}'|}, \tag{A.8}$$

$$v_{xc}(\mathbf{r}) = \frac{\delta E_{xc}}{\delta n(\mathbf{r})}. \tag{A.9}$$

These are the *KS equations*, whose solution is found via a self–consistent iterative procedure: starting from a given set of $\psi_i(\mathbf{r})$ we determine the density and the potential $V_{KS}(\mathbf{r})$, and then we solve the Eq. (A.7) to determine new orbitals $\psi_i(\mathbf{r})$. This cycle is repeated, using the new orbitals as input wavefunctions, until the input and the output orbitals are identical.

A.2 Local Density Approximation

The DFT described above is formally exact but useless for practical purposes, because all difficulties related to the many–body character of the problem are still unsolved. They are all contained in the exchange–correlation energy $E_{xc}[n]$, which is formally well defined by the equation (A.6) but unknown. In order to apply the theory an appproximation for $E_{xc}[n]$ is necessary. The most common and simplest approach is the *local density* approximation (LDA). It relies on the

idea of replacing the exchange–correlation energy of a non uniform interacting electron system with the $E_{\rm xc}[n]$ computed as if locally it had the same exchange–correlation energy of a *uniform* interacting system with the same density:

$$E_{\rm xc}^{LDA} = \int d\mathbf{r} \epsilon_{\rm xc}^{hom}[n(\mathbf{r})] n(\mathbf{r}), \tag{A.10}$$

where $\epsilon_{\rm xc}^{hom}[n(\mathbf{r})]$ is the exchange–correlation energy per particle of a homogeneous electron gas with density $n(\mathbf{r})$. This quantity depends locally upon the density at the point $\mathbf{r}$ and it has been determined with high accuracy using quantum Monte Carlo simulations [34] which provided the total ground–state energy of the uniform interactins electron gas at several densities. These energies have been interpolated by several authors. For our computations we have chosen the recipe of Perdew and Zunger [130].

The LDA approximation, free of experimental input, is exact only in the limit of uniform systems, and its application is formally justified for systems with slowly varying electron density. Somewhat surprisingly, the application of the LDA approximation to a large variety of systems has shown that this approximation reproduces satisfactorily many measurable quantities, including ground–state structures of molecules and solids, vibrational properties, etc.

A.3 Plane–Wave Pseudopotential Method

In the study of infinite solids it is necessary to exploit the crystal symmetry to circumvent the problem of the infinite number of degrees of freedom. The Bloch theorem states that in a periodic crystal the electronic wavefunctions are given by the product of a function having the lattice periodicity times a plane–wave.

In order to solve in practice the KS equations, one can write the KS orbitals in terms of a suitable finite basis set. A standard choice is that of using plane–waves (PW), which have the great advantage of being translationally invariant:

$$\psi_i(\mathbf{r}) = \psi_{n,\mathbf{k}}(\mathbf{r}) = \sum_{\mathbf{G}} c_{n,\mathbf{k}+\mathbf{G}} e^{i(\mathbf{k}+\mathbf{G})\cdot\mathbf{r}} \tag{A.11}$$

where $\mathbf{k}$ belongs to the first Brillouin Zone (BZ) of the crystal, $\mathbf{G}$ is a reciprocal lattice vector, and n is the band index. The use of Bloch functions would then

require the knowledge of the electronic wavefunctions at every point in the first BZ of the reciprocal lattice. Nevertheless, efficient k-sampling methods have been proposed by different authors [38, 131, 132], where very restricted sets of "special points" are taken as representative of the entire zone.

The electronic density is then calculated self-consistently through Eq. (A.5). For insulating systems at zero temperature the occupation of the Bloch states can be fixed to two or zero electrons per spin–degenerate state. In metals, a fractional occupation of states at the sampling k-points close to the Fermi energy is commonly introduced to mimic the properties of the Fermi surface. The calculations reported in this thesis employ the smearing technique [133] to deal with BZ integration in the presence of a Fermi surface.

The dimension of the PW basis set is determined by fixing the kinetic energy cut–off, E_{cut}, through the condition:

$$\frac{1}{2}|\mathbf{k}+\mathbf{G}|^2 \leq E_{cut}. \tag{A.12}$$

The choice of a PW basis has the advantage that the matrix elements of the Hamiltonian in Eq. (A.7) are particularly simple and that the accuracy of the expansion can be easily checked and systematically improved by increasing the value of E_{cut}; furthermore, PW's are independent of the structure of the crystal.

Unfortunately only a very large PW basis is able to accurately reproduce the rapid spatial variation of the orbitals in the region around the nuclei. However, the orbitals closer to the nuclei (the *core* orbitals) are very well localized, energetically well separated from all valence states, and they do not play a role in the interatomic bonds, *i.e.* in most properties of the system. These considerations justify the elimination, from the KS equations, of the degrees of freedom associated with the core electrons, and only the "chemically active" electrons are explicitly included in the computation.

The switch from the all–electron problem to an equivalent problem that involves only the valence electrons is exploited by replacing the nuclear potential $V_{\text{ext}}(\mathbf{r})$ in the Hamiltonian (A.1), with a smooth *pseudopotential* describing the interaction between valence electrons and ionic cores (nuclei + core electrons). There are many different schemes to generate ionic pseudopotentials from first principles (see for example [117, 134]). Basically, all of them satisfy the follow-

ing requirements: (*i*) the lowest pseudo–energy levels are equal to the valence all–electron energies; (*ii*) each pseudo–wave function coincides with the corresponding all–electron one outside a properly chosen core radius; (*iii*), the real and pseudo charge inside the core radius agree for each valence state (as a consequence of (*ii*)). This last condition is called *norm conservation*, and ensures the transferability of the pseudopotential to different chemical environments [135]. The accuracy of the results obtained with norm–conserving pseudopotentials is comparable with those from all–electron calculations [21, 136]. The price to be payed for norm conservation is nonlocality, which shows up in the explicit l-dependence of the radial ionic pseudopotential. A computationally convenient form for the pseudopotential has been introduced by Kleinman and Bylander [39], who pointed out that a significant reduction of the numerical effort can be achieved if the nonlocality of the potential is not restricted to the angular part, but if also the radial potential is replaced by a suitable non local separable operator. The Kleinman–Bylander form must be used with some caution, because in some cases it can lead to a wrong description of the chemical properties of the system, due to the appareance of unphysical states in the energy spectrum of the isolated atom. These spurious states, known in literature as *ghosts* [137], may occur because—due to the non locality of the radial potential—is no longer guaranteed that the radial wavefunctions can be ordered in terms of the increasing number of their nodes. In particular, the nodeless radial pseudo–functions, which are assumed to describe the relevant atomic states for different angular numbers, are not necessarily the ground–states of the pseudo–Hamiltonian from which they are obtained.

The description of cases in which the crystal symmetry is broken, as in surfaces, quantum–confined systems, amorphous solids, isolated molecules and so on, needs the construction of larger cells ("supercells") that introduce a fictitious periodicity in the system. The computational cost of DFT *ab initio* calculations grows approximately with the third power of the number of electrons. At present, systems containing up to a few tens of inequivalent atoms can be simulated on big workstations, while larger supercells with a couple of hundreds of particles are dealt with by using parallel supercomputers.

Appendix B

Ab–initio Molecular Dynamics

B.1 Classical and quantum molecular dynamics

We focus on the ionic degrees of freedom, considering the evolution of the ionic coordinates, with the aim of simulating dynamical processes and/or of determining the most stable structures.

Molecular Dynamics (MD) methods have been described extensively by several authors [138], and we restrict ourselves to the basic concepts. The time evolution of a system of M classical particles is governed by the Lagrangian:

$$\mathcal{L} = T - V. \tag{B.1}$$

Usually the kinetic energy T takes the form:

$$T = \sum_{I=1}^{M} \frac{1}{2} m_I \dot{\mathbf{q}}_I{}^2, \tag{B.2}$$

where $\dot{\mathbf{q}}_I$ and m_I are the velocity and the mass of the I-th particle, respectively. The potential energy V contains the interesting information regarding the interactions between the particles. Once the expression for V is given, we can compute the forces on the particles:

$$\mathbf{F}_I = -\nabla_{\mathbf{q}_I} V, \tag{B.3}$$

and solve the Newton's equations of motions, which give the time evolution of the system.

The key to an accurate description of system is the set–up of a reliable expression for a potential V. In the *classical* molecular dynamics approach, the "real" potential is modelled by an effective potential containing adjustable parameters that are fitted to reproduce measured or computed quantities. In many cases of interest, however, these simple models are not able to provide a reliable description of the "real" potential surface. They fail, for example, to describe the breaking or forming of bonds, or in the description of systems whose chemical or physical state changes. An adequate description of these phenomena must explicitly take into account the electronic structure.

According to DFT, we can calculate the potential V acting on the ions by solving the instantaneous electronic problem. In fact, this potential is given by:

$$V(\{\mathbf{R}_I\}) = \min_{\{\psi_i\}} E_{\rm tot}[\{\psi_i\}, \{\mathbf{R}_I\}], \tag{B.4}$$

where $E_{\rm tot}$ is obtained by adding the potential energy of the ion–ion interaction to the KS expression for the total energy of the electronic system:

$$E_{\rm tot}[\{\psi_i\}, \{\mathbf{R}_I\}] = -\frac{1}{2}\sum_{i}^{occ}\langle\psi_i(\mathbf{r})|\nabla^2|\psi_i(\mathbf{r})\rangle + \int d\mathbf{r} V_{\rm ext}(\mathbf{r})n(\mathbf{r}) + \\ + \frac{1}{2}\int d\mathbf{r}d\mathbf{r}'\frac{n(\mathbf{r})n(\mathbf{r}')}{|\mathbf{r}-\mathbf{r}'|} + E_{\rm xc}[n] + \frac{1}{2}\sum_{I\neq J}\frac{Z_I Z_J}{|\mathbf{R}_I - \mathbf{R}_J|}. \tag{B.5}$$

Therefore, a combined DFT/MD scheme can be implemented where the time evolution of the ions is governed by the potential, free of adjustable parameters, produced by the DFT electronic structure optimization. An advantage of combining the two schemes is that parameter–free potentials are general and versatile, and represent a significant improvement over the potentials fitted to reproduce experimental and/or theoretical data. A molecular dynamics with DFT–based interatomic potentials could be performed in the following way:

(1) begin with a likely configuration of the ions,

(2) solve the KS equations for this ionic configuration,

(3) use the electronic structure and the Hellmann–Feyman theorem [139] to calculate the forces on the ions,

(4) move the ions according to the classical equation of motion,

(5) take the new ionic coordinates, go to step (2) and continue.

Although this procedure is conceptually possible, it is not practicable. The solution of the electronic–structure problem according to the DFT requires matrix diagonalization calculations, which must be iterated until the self–consistency is reached. These computations have a relevant computational burden, and if this time is multiplied by the number of the ionic configurations visited during the dynamical process (of the order of 10^4–10^5), it becomes evident that only very small systems could be studied with this method.

B.2 The Car–Parrinello method

The success of combined DFT/MD calculations is due to a different approach introduced in 1985 by Car and Parrinello [75]. The idea on which the Car–Parrinello (CP) method is based is to consider a fictitious dynamical system where the ionic and electronic degrees of freedom are treated on the same footing. This is achieved associating a fictitious classical kinetic energy to the electronic degrees of freedom (the KS orbitals $\psi_i(\mathbf{r})$), i.e. adding a kinetic energy term for the electrons in the Lagrangian of the system. The Lagrangian reads then:

$$\begin{aligned} \mathcal{L} &= \mu \sum_{i}^{occ} \int d\mathbf{r} |\dot{\psi}_i(\mathbf{r})|^2 + \frac{1}{2} \sum_I m_I \dot{\mathbf{R}}_I^2 - E_{\rm tot}[\{\psi_i\}, \{\mathbf{R}_I\}] + \\ &+ \sum_{ij} \Lambda_{ij} \Big(\int d\mathbf{r}\, \psi_i^*(\mathbf{r}) \psi_j(\mathbf{r}) - \delta_{ij} \Big). \end{aligned} \tag{B.6}$$

Here μ is the fictitious electron mass, m_I are the ionic masses, and Λ_{ij} are the Lagrangian multipliers arising from the orthonormality constraint on the $\psi_i(\mathbf{r})$, which must be satisfied at any time t during the dynamical process. The equations of motion associated with the Lagrangian $\mathcal{L}$ are:

$$\mu \ddot{\psi}_i(\mathbf{r}, t) = -\frac{\delta E_{\rm tot}}{\delta \psi_i^*(\mathbf{r}, t)} + \sum_j \Lambda_{ij} \psi_j(\mathbf{r}, t) \tag{B.7}$$

and

$$m_I \ddot{\mathbf{R}}_I = -\nabla_{\mathbf{R}_I} E_{\rm tot}. \tag{B.8}$$

The dynamics is then performed in the following way:

(1) start from a likely ionic configuration,

(2) solve the electron–structure problem, *i.e.* calculate

$$\min_{\{\psi_i\}} E_{\rm tot}[\{\psi_i\}, \{\mathbf{R}_I\}], \tag{B.9}$$

(3) compute the forces on ions ($\nabla_{\mathbf{R}_I}\mathcal{L}$) and electrons ($\delta_{\psi^*}\mathcal{L}$)

(4) move electronic wavefunctions and ions *simultaneously*, go to step (3) and continue.

In other words, the fictitious electronic optimization dynamics and the proper ionic dynamics are run in parallel: in the same time–step the ions are moved according to the self–consistent forces, while the electron variables are moved according to the energy gradients and constraints. In this way the costly electronic–structure calculations at every step of the ionic motion are replaced by *only one* initial optimization of the electronic wavefunctions and by their relatively inexpensive update at each MD step. The fictitious electron dynamics and the assumption $\mu \ll m_I$ prevent energy transfer from the ionic to the electronic degrees of freedom over the time scale of the simulation, so that the electronic wavefunction are automatically updated to follow *adiabatically* the nuclear motion, *i.e.* they remain in their ground–state.

Since its establishment, the CP method has extended the range of conventional electronic–structure calculations, and it has been applied to a great variety of problems. Examples are the determination of physical properties of disordered systems, the study of relevant dynamical processes in the area of semiconductors, surface reconstruction, atomic clusters and more. This method, born and traditionally applied in the realm of solid state physiscs, has recently attracted the attention of the quantum chemists, and it is increasingly used to study chemical reactions and even biological systems. Further details about this method and its applications can be read in numerous review articles published in the last decade [76–81].

Bibliography

[1] W. Kohn, Phys. Rev. **133**, A171 (1964).

[2] A. D. Becke, K. E. Edgecombe, J. Chem. Phys. **92**, 5397 (1990).

[3] A. Savin, O. Jepsen, J. Flad, O. K. Andersen, H. Preuss and H. G. von Schneiring, Angew. Chem. Int. Ed. Engl. **31**, 187 (1992).

[4] B. Silvi, A. Savin, Nature **371**, 683 (1994).

[5] A. Savin, A. D. Becke, J. Flad, R. Nesper, H. Preuss and H. G. von Schnering, Angew. Chem. Int. Ed. Engl. **30**, 409 (1991).

[6] A. Savin, R. Nesper, S. Wengert and T. F. Fässler, Angew. Chem. Int. Ed. Engl. **36**, 1808 (1997).

[7] M. Kohout, A. Savin, J. Flad, H. Preuss and H. G. von Schneiring, in *Computer Aided Innovation of New Materials II* edited by M. Doyama, J. Kihara, M. Tanaka, R. Yamamoto (Elsevier, Amsterdam, 1993), p. 201.

[8] N. Marzari and D. Vanderbilt, Phys. Rev. B **56**, 12847 (1997).

[9] R. Resta and S. Sorella, Phys. Rev. Lett. **82**, 370 (1999).

[10] C. Sgiarovello, thesis, University of Trieste, 1999; C. Sgiarovello, M. Peressi, and R. Resta, *unpublished.*

[11] L. De Santis and R. Resta, Solid State Commun. **106**, 763 (1998).

[12] L. De Santis and R. Resta, Solid State Commun. **111**, 583 (1999).

[13] L. De Santis and R. Resta, *submitted for pubblication.*

[14] M. Peressi, M. Fornari, S. de Gironcoli. L. De Santis, and A. Baldereschi, Phil. Mag. B, *in press.*

[15] Y. Tal, R. F. W. Bader, Int. J. Quantum Chem. Symp. **12**, 153 (1978).

[16] R. M. Dreizler and E. K. U. Gross, *Density Functional Theory: an Approach to the Quantum Many–Body Problem* (Springer–Verlag, Berlin, 1990).

[17] M. L. Cohen, in *Electronic Materials*, edited by J. R. Chelikowsky and A. Franciosi (Springer–Verlag, Berlin, 1991), p.57.

[18] P. Hohenberg and W. Kohn, Phys. Rev. **136** B864 (1964).

[19] W. Kohn and L. J. Sham, Phys. Rev. **140**, A1133 (1965).

[20] *Theory of the Inhomogeneous Electron Gas,* edited by S. Lundqvist and N. H. March (Plenum Press, New York, 1983).

[21] W. E. Pickett, Comput. Phys. Rep. **9**, 115 (1989).

[22] M. Kohout and A. Savin, J. Comp. Chem. **18**, 1431 (1997).

[23] W. A. Harrison, *Pseudopotentials in the Theory of Metals* (Benjamin, New York, 1966).

[24] V. Heine, in *Solid State Physics*, edited by H. Ehrenreich, F. Seitz, and D. Turnbull, vol. **24** (Academic, New York, 1970), p.1; M. L. Cohen and V. Heine, *ibid.* p.250.

[25] J. C. Phillips, Rev. Mod. Phys. **42**, 317 (1970); *Bonds and Bands in Semiconductors*, (Academic Press, New York, 1973).

[26] L.H. Thomas, Proc. Camb. Phil. Soc. **23**, 542 (1927); E. Fermi, Z. Phys. **48**, 73 (1928). Reprinted in N. H. March *Self–Consistent Fields in Atoms* (Pergamon, Oxford, 1975).

[27] J. E. Harriman, Phys. Rev. A **24**, 680 (1981).

[28] G. Zumbach and K. Maschke, Phys. Rev. A **28**, 544 (1983).

[29] E. V. Ludeña, J. Chem. Phys. **79**, 6174 (1983).

[30] For a recent review, see: E. V. Ludeña, R. López–Boada, and R. Pino, Can. J. Chem. **74**, 1097 (1996).

[31] R. López–Boada, E.V. Ludeña, V. Karasiev, R. Pino, J. Chem. Phys. **107**, 6722 (1997).

[32] F. Gygi, Europhys. Lett. **19**, 617 (1992).

[33] F. Gygi, Phys. Rev. B **48**, 11692 (1993).

[34] D. M. Ceperley and B. J. Alder, Phys. Rev. Lett. **45**, 566 (1980).

[35] G. Ortíz and P. Ballone, Phys. Rev.**50**, 1391 (1994).

[36] T. F. Fässler, U. Häussermann and R. Nesper, Chem. Eur. J. **1**, 625 (1995).

[37] J. Dabrowski and M. Scheffler, Appl. Surf. Sci. **56–58**, 15 (1992).

[38] H. J. Monkhorst and J. D. Pack, Phys. Rev. B **13**, 5188 (1976).

[39] L. Kleinman, and D. M. Bylander, Phys. Rev. Lett. **48**, 1425 (1982).

[40] N. Roberts and R. J. Needs, Surf. Sci. **236**, 112 (1990).

[41] C. J. Fall, N. Binggeli, and A. Baldereschi, Phys. Rev. B **58**, R7544 (1998).

[42] L. Ley in *The Physics of Hydrogenated Amorphous Silicon II*, edited by J. Joannopulos and L. Lucovsky (Springer–Verlag, Berlin, 1984), p. 61.

[43] P. A. Fedders and A. E. Carlsson, Phys. Rev. B **37**, 8506 (1988).

[44] P. A. Fedders and A. E. Carlsson, Phys. Rev. B **39**, 1134 (1989).

[45] R. Biswas, C. Wang, C. Chan, K. Ho, and C. Soukoulis, Phys. Rev. Lett. **63**, 1491 (1989).

[46] J. Holender, G. Morgan and R. Jones, Phys. Rev. B **47**, 3991 (1993).

[47] Lee In-Ho and K. J. Chang, Phys. Rev. B **50**, 18083 (1994).

[48] E. A. Davis, Journal of Non–Cryst. Sol. **198-200**, 1 (1996).

[49] B. Tuttle and J. B. Adams, Phys. Rev. B **53**, 16265 (1996).

[50] S. T. Pantelides, Phys. Rev. Lett. **57**, 2979 (1986).

[51] S. T. Pantelides, Phys. Rev. Lett. **58**, 1344 (1987).

[52] P. C. Kelires and J. Tersoff, Phys. Rev. Lett. **61**, 562 (1988).

[53] F. Buda, G. L. Chiarotti, I. Štich, R. Car and M. Parrinello, J. Non–Cryst. Sol. **114**, 7 (1989).

[54] I. Štich, R. Car and M. Parrinello, Phys. Rev. B **44**, 11092 (1991).

[55] F. Buda, G. L. Chiarotti, R. Car and M. Parrinello, Phys. Rev. B **44**, 5908 (1991).

[56] P. A. Fedders and A. E. Carlsson, Phys. Rev. Lett **58**, 1156 (1987).

[57] P. A. Fedders, D. A. Drabold, S. Klemm, Phys. Rev. B **45** 4048 (1992).

[58] M. Fornari, M. Peressi, S. de Gironcoli and A. Baldereschi, to be published.

[59] G. A. Jeffrey, W. Saenger, *Hydrogen bonding in biological structures* (Springer–Verlag, Berlin, 1991).

[60] W. W. Cleland, Biochemistry **31**, 317 (1992).

[61] W. W. Cleland and M. M. Kreevoy, Science **264**, 1887 (1994).

[62] J. A. Gerlt and P. G. Gassman, Biochemistry **32**, 11934 (1993).

[63] J. A. Gerlt and P. G. Gassman, J. Am. Chem. Soc. **115**, 11552 (1993).

[64] W. W. Cleland, P. A. Frey and J. A. Gerlt, J. Biol. Chem. **273**, 25529 (1998).

[65] C. L. Perrin, Science **266**, 1665 (1994).

[66] P. A. Frey, S. A. Whitt, J. B. Tobin, Science **264**, 1927 (1994).

[67] L. Pauling, Chem. Eng. News **24**, 1375 (1946).

[68] V. L. Schramm, Annu. Rev. Biochem. **67**, 693 (1998).

[69] L. De Santis and P. Carloni, PROTEINS: Struc. Func. Gen., *in press.*

[70] S. Pantano, F. Alber, and P. Carloni, *to be submitted.*

[71] F. Alber and P. Carloni, *to be submitted.*

[72] J. Lin, W. M. Westler, W. W. Cleland, J. L. Markley, P. A. Frey, Proc. Natl. Acad. Sci. USA **95**, 14664 (1998).

[73] J. Lin, C. S. Cassidy, P. A. Frey, Biochemistry **37**, 11940 (1998).

[74] C. S. Cassidy, J. Lin, P. A. Frey, Biochemistry **36**, 4576 (1997).

[75] R. Car, M. Parrinello, Phys. Rev. Lett. **55**, 2471 (1985).

[76] R. Car and M. Parrinello, in *Simple Molecular Systems at Very High Density*, edited by A. Polian, L. Loubeyre, and N. Boccara (Plenum–Press, New York, 1988), p. 455.

[77] G. Galli and M. Parrinello, in *Computer Simulations in Material Science*, edited by M. Meyer and V. Pontikis (Plenum–Press, New York, 1991), p. 283.

[78] M. C. Payne, M. P. Teter, D. C. Allen, T. A. Arias, and J. D. Joannopoulos, Rev. Mod. Phys. **64**, 1045 (1992).

[79] G. Galli and A. Pasquarello, in *Computer Simulations in Chemical Physics*, edited by M. P. Allen and T. J. Tildesley (Kluwer Academic Publisher, Dodrecht, 1993).

[80] D. K. Remler and P. Madden, Mol. Phys. **70**, 921 (1990).

[81] M. Parrinello, Solid State Commun. **102**, 107 (1997).

[82] U. Roethlisberger and P. Carloni, Int. J. Quantum Chem. **73**, 209 (1999).

[83] F. Alber, O. Kuonen, L. Scapozza, G. Folkers, P. Carloni, PROTEINS: Struc. Func. Gen., **31**, 453 (1998).

[84] C. Molteni, M. Parrinello, J. Am. Chem. Soc. **120**, 2168 (1998).

[85] F. Alber, G. Folkers and P. Carloni, J. Mol. Struc. (Theochem), *in press.* (1999).

[86] P. Gilli, V. Bertolasi, V. Ferretti, G. Gilli, J. Am. Chem. Soc. **116**, 909 (1994).

[87] B. Schiott, B. B. Iversen, G. K. Madsen, F. K. Larsen, T. C. Bruice, Proc. Natl. Acad. Sci. USA **95**, 12799 (1998).

[88] C. L. Perrin amd J. B. Nielson, Annu. Rev. Phys. Chem. **48**, 511 (1997).

[89] A. Warshel, A. Papazyan, P. A. Kollman, Science **269**, 102 (1995).

[90] A. Warshel, J. Biol. Chem. **273**, 27035 (1998).

[91] S. N. Rao, U. C. Singh, P. A. Bash and P. A. Kollman, Nature **328**, 551 (1987).

[92] J. K. Hwang, A. Warshel, Biochemistry **26**, 2669 (1987).

[93] A. Warshel, S. Russell, J. Am. Chem. Soc. **108**, 6569 (1986).

[94] A. Warshel and A. Papazyan, Proc. Natl. Acad. Sci. USA **93**, 13665 (1996).

[95] J. Kraut, Annu. Rev. Biochem. **46**, 331 (1977).

[96] R. M. Stroud, Sci. Am. **231**, 74 (1974).

[97] N. R. Matheson, H. van Halbeek, J. Travis, J. Biol. Chem. **266**, 13489 (1991).

[98] T. A. Steitz, R. G. Shulman, Annu. Rev. Biochem. Biophys. **11**, 419 (1982).

[99] H. Neurath and K. A. Walsh, Proc. Natl. Acad. Sci. U.S.A. **73**, 3825 (1976).

[100] H. Neurath, Science **224**, 350 (1984).

[101] G. Dodson and A. Wlodawer, Trends Biochem. Sci. **23**, 347 (1998).

[102] D. M. Blow, J. J. Birktoft, B. S. Hartley, Nature **221**, 337 (1969).

[103] B. W. Matthews, P. B. Sigler, R. Henderson, D. M. Blow, Nature **214**, 652 (1967).

[104] L. Stryer, *Biochemistry*, 3rd ed. (W. H. Freeman and Company, New York, 1988).

[105] T. E. Creighton, *Proteins: structures and molecular properties*, 2nd ed. (W. H. Freeman and Company, New York, 1993).

[106] C. Branden, J. Tooze, *Introduction to protein structure*, 2nd ed. (Garland, New York, 1999).

[107] A. Fersht, *Enzyme structure and mechanism*, 2nd ed. (W. H. Freeman, New York, 1985).

[108] P. Bryan, M. W. Pantoliano, S. G. Quill, H. Y. Hsiao, T. Poulos, Proci. Natl. Acad. Sci. USA **83**, 3743 (1986).

[109] A. Warshel, G. Naray–Szabo, F. Sussman and J. K. Hwang, Biochemistry **28**, 3629 (1989).

[110] J. A. Wells, B. C. Cunningham, T. P. Craycar and D. A. Estell, Phil. Trans. R. Soc. Lond. A **317**, 415 (1986).

[111] F. C. Bernstein, T. F. Koetzle, G. J. B. Williams, *et al.* J. Mol. Biol. **112**, 535 (1977).

[112] C. J. Halkides, Y. Q. Wu, C. J. Murray, Biochemistry **35**, 15941 (1996).

[113] L. H. Takahashi, R. Radhakrishnan, R. E. Rosenfield, E. F. Meyer, D. A. Trainor, J. Am. Chem. Soc. **111**, 3368 (1989).

[114] D. A. Case, D. A. Pearlman, J. W. Caldwell, T. E. Cheatham III, W. S. Ross, C. L. Simmerling, T. A. Darden, K. M. Merz, R. V. Stanton, A. L. Cheng, J. J. Vincent, M. Crowley, D. M. Ferguson, R. J. Radmer, G. L. Seibel, U. C. Singh, P. K. Weiner, P. A. Kollman, AMBER5 (University of California, San Francisco, 1997).

[115] W. D. Cornell, P. Cieplak, C. I. Bayly, I. R. Gould, K. M. Merz Jr., D. M. Ferguson, D. C. Spellmeyer, T. Fox, J. W. Caldwell, P. A. Kollman, J. Am. Chem. Soc. **117**, 5179 (1995).

[116] R. E. Babine, S. L. Bender, Chem. Rev. **97**, 1359 (1997).

[117] N. Troullier and J. L. Martin, Phys. Rev. B **43**, 1993 (1991).

[118] A. D. Becke, Phys. Rev. A **38**, 3098 (1988).

[119] C. L. Lee, W. Yang and R. G. Parr, Phys. Rev. B **37**, 785 (1988).

[120] P. Pulay, Chem. Phys. Lett. **73**, 393 (1980).

[121] J. Hutter, H. P. Lüthi, M. Parrinello, Comput. Mater. Sci. **2**, 244 (1994).

[122] S. Nosé, J. Chem. Phys. **81**, 511 (1981).

[123] W. D. Cornell, P. Cieplak, C. I. Bayly, P. A. Kollman, J. Am. Chem. Soc. **115**, 9620 (1993).

[124] S. R. Cox and D. E. Williams, J. Comput. Chem. **2**, 304 (1982).

[125] J. Hutter, P. Ballone, M. Bernasconi, P. Focher, E. Fois, S. Goedecker, M. Parrinello, M. Tuckerman, CPMD version 3.0h. (MPI für Festkörperforschung and IBM Zurich Research Laboratory, 1995-98).

[126] M. Born and R. Oppenheimer, Ann. Phys. **84**, 457 (1927).

[127] M. Born and K. Huang, *Dynamical Theory of Crystal Lattices*, (Clarendon Press, Oxford, 1954).

[128] R. G. Parr and W. Yang, *Density Functional Theory of Atoms and Molecules* (Oxford University Press, New York, 1989).

[129] R. O. Jones and O. Gunnarson, Rev. Mod. Phys. **61**, 689 (1989).

[130] J. Perdew and A. Zunger, Phys. Rev. B **23**, 5048 (1981).

[131] A. Baldereschi, Phys. Rev. B **7**, 5212 (1973).

[132] D. J. Chadi and M. L. Cohen, Phys. Rev. B **8**, 5747 (1973).

[133] M. Methfessel and A. T. Paxton, Phys. Rev. B **40**, 3616 (1989).

[134] G. B. Bachelet, D. R. Hamann and M. Schlüter, Phys. Rev. B **26**, 4199 (1982).

[135] D. R. Hamann, M. Schlüter and C. Chiang, Phys. Rev. Lett. **43**, 1494 (1979).

[136] G. B. Bachelet and N. C. Christensen, Phys. Rev. B **8**, 5747 (1973).

[137] X. Gonze, P. Käckell and M. Scheffler, Phys. Rev. B **41**, 12264 (1990).

[138] M. P. Allen and T. J. Tildesley, *Computer Simulations of Liquids* (Clarendon–Press, Oxford, 1987).

[139] P. Ehrenfest, Z. Phys. **45**, 455 (1927); R. P. Feynman, Phys. Rev. **56**, 340 (1939).